Invited Topical Review: P-type transparent conducting oxides

Kelvin H L Zhang[1], Kai Xi[1], Mark G Blamire[1] and Russell G Egdell[2]

[1] Department of Materials Science & Metallurgy, University of Cambridge, 27 Charles Babbage Road, Cambridge, CB3 0FS, UK

[2] Department of Chemistry, University of Oxford, Inorganic Chemistry Laboratory, South Parks Road, Oxford OX1 3QR, UK

Abstract: Transparent conducting oxides constitute a unique class of materials combining properties of electrical conductivity and optical transparency in a single material. They are needed for a wide range of applications including solar cells, flat panel displays, touch screening, light emitting diodes and transparent electronics. Most of the commercially available TCOs are *n*-type, such as Sn doped In_2O_3, Al doped ZnO, and F doped SnO_2. However, the development of efficient *p*-type TCOs remains an outstanding challenge. This challenge is thought to be due to the localized nature of the O 2*p* derived valence band which leads to difficulty in introducing shallow acceptors and large hole effective masses. In 1997 Hosono and co-workers (Nature ***1997***, 389 939) proposed the concept of "chemical modulation of the valence band" to mitigate this problem using hybridization of O 2*p* orbitals with close-shell Cu $3d^{10}$ orbitals. This work has sparked tremendous interests in designing p-TCO materials together with deep understanding the underlying materials physics. In this article, we will provide a comprehensive review on traditional and recently emergent p-TCOs, including Cu^+-based delafossites, layered oxychalcogenides, nd^6 spinel oxides, Cr^{3+}-based oxides ($3d^3$) and post-transition metal oxides with lone pair state (ns^2). We will focus our discussions on the basic materials physics of these materials in terms of electronic structures, doping and defect chemistry for p-type conductivity and optical properties. Device applications based on p-TCOs for transparent p-n junctions will also be briefly discussed.

Outline:

1. Introduction to transparent conducting oxides (TCOs)
2. Brief materials physics of TCOs
   - 2.1 Electrical conductivity and electronic structure
   - 2.2 Optical properties
   - 2.3 Figure of merits
   - 2.4 Design rules for p-type TCOs
3. Cu^{+}-based materials ($3d^{10}$)
   - 3.1 Cu_2O
   - 3.2 Delafossite ($CuMO_2$)
     - 3.2.1 Crystal structure and thin film growth
     - 3.2.2 Electronic and optical properties
     - 3.3 $SrCu_2O_2$
4. Layered oxychalcogenides
5. Spinel oxides (nd^6)
6. Cr-based oxides ($3d^3$)
7. Lone pair based oxide (ns^2)
8. NiO ($3d^8$)
9. Summary and remarks

1. Introduction to transparent conducting oxides (TCOs)

Electrical conductivity and optical transparency are seemingly mutually exclusive properties when considering conventional solid state materials such as metals, semiconductors and ceramics. Metals are conductive but opaque due to the free electrons at the Fermi level; semiconductors such as Si and GaAs are semi-conducting but showing strong absorption for visible light; ceramics are generally transparent but insulating due to their large bandgap. Transparent conducting oxides (TCOs) are a class of materials displaying a combination of a close-to 'metallic' ($\sim 10^4$ S cm^{-1}) and almost "insulating" transparency (>80%) in the visible light range, achieved by degenerately doping of wide bandgap oxide semiconductors. Because of such unique properties, TCOs form the basis of numerous important applications in contemporary and emerging technologies.[1-4] A typical example is the use of TCOs as transparent electrodes for touch screen in smart phones, liquid crystal displays, organic light emitting diodes and solar cells.[3-7] Emerging technologies include using TCOs as active layers for transparent thin film transistors,[8-11] UV light emitting diodes and detectors,[12] and gas sensors.[13-15]

The literature on TCOs is vast, testifying to more than 100 years of intensive scientific investigation and technical application. The first TCO thin film, cadmium oxide (CdO), was made by Badeker in 1907 *via* thermally oxidizing a vacuum sputtered film of Cd metal.[16] However CdO is not widely used today because of toxicity issue, whereas it is still of scientific interest because of its high electron mobility.[17, 18] The first large-scale use of TCOs occurred during World War II, when antimony-doped tin oxide (Sb:SnO_2) coating was used as a transparent defroster for aircraft windshields.[19] Electrical heating of windshields and windows in aircraft and vehicles is still an important application of TCOs until now. To date, the industry standards TCOs are n-type degenerately doped wide bandgap post-transition metal oxides, including Sn-doped In_2O_3, F-doped SnO_2 and Al-doped ZnO, where the ionic

character of the parent oxides produces an oxygen 2p-derived valence band (VB) and the metal *s* orbital derived conduction band (CB), resulting in large optical band gaps (>3.1 eV) and concomitantly an excellent n-type conductivity when donors doped.[20, 21] Sn-doped In_2O_3 (also called indium-tin-oxide or ITO) accounts for more than 90 percent of the display market, and has been the dominant material for the past 60 years.[5] The materials used in industry are usually in the form of polycrystalline or amorphous thin films deposited on glass or polymer substrates by sputtering techniques. ITO thin films have the advantage of a high conductivity up to ~10^4 $S \cdot cm^{-1}$, a transmittance of greater than 80% and ease to fabrication. However the low abundance and the ramping price of indium raw metal have significantly increased the cost of ITO by 1000% in recent 10 years. Therefore intensive research efforts from both academia and industry have been devoted to exploiting F-doped SnO_2, Al-doped ZnO, and graphene[22] as possible alternatives to ITO.[5, 6]

On the other hand, many potential applications of TCOs are still limited by the lack of their p-type counterparts.[2, 12, 23, 24] A high performance p-type TCOs would leverage the great promise of oxides for transparent electronics and optoelectronics by combining with the common n-type ones into p-n heterojunctions. The recent rapid development of photovoltaics and solar water splitting also calls for calls for *p*-type electrodes for more efficient hole collection.[3] The challenge in achieving p-type TCOs is due to the intrinsic electronic structure of metal oxides: the top of VB of most oxide materials is comprised of strongly localized O 2*p*-derived orbitals.[25, 26] Oxygen is a relatively small atom with a high electronegativity, leading to difficulty in introducing shallow acceptors and large hole effective masses. In 1997, Hosono and co-workers proposed the concept of "chemical modulation of the valence band" (CMVB) to mitigate this problem using hybridization of O 2*p* orbitals with closed-shell Cu $3d^{10}$ orbitals.[25] Because the Cu $3d^{10}$ level is close to that of an O $2p^6$ level, it is expected that the Cu $3d^{10}$ can form strong covalent bonding with O $2p^6$. This will result in a

large dispersion at the top of VB and reduction of the localization of positive holes. Meanwhile the closed shell d^{10} also avoids coloration due to *d-d* excitations, ensuring the optical transparency for visible light. Following this design rule, a series of p-TCOs based on Cu^+ bearing oxides, such as delafossites $CuMO_2$ (M = Al[25, 27], Cr[28, 29], In[30], Sc[31], Y[32] and Ga[33]) and $SrCu_2O_2$[34] have been discovered. With p-type TCO materials identified, the fabrication of a transparent p-n junction made exclusively from TCO materials became possible.[35] Besides exploring the Cu 3d-O 2p interaction to enhance VB dispersion, the concept of CMVB was extended to use chalcogens (Ch= S, Se, and Te) to replace the oxygen, since more hybridization between the Cu 3d orbitals and the Ch p orbitals was expected in the sequence of O, S, Se, and Te. Layered LaCuOCh (Ch=S and Se)[36-39] and $Sr_3Cu_2Sc_2O_5S_2$[40] are the two most promising p-TCOs identified following this rule. To date Mg-doped LaCuOSe exhibit the highest p-type conductivity of 910 S cm^{-1}, but unfortunately the small bandgap of LaCuOSe (2.8 eV) limits its optical transparency.[38] More recently, CMVB has also been applied to other materials with quasi-closed shells such as d^6 and d^3. This leads to the identification of a serial of new p-TCOs such as ZnM_2O_4 spinels and Cr-based oxides.[41] Compared to layered Cu^+-based materials, the new p-TCOs normally have three dimensional lattice structures and are more compatible to integrate with the existing n-type materials. Furthermore, cation s states are generally more delocalized than d states, and their hybridization with O 2p states can result in lighter hole effective mass. This can be realized in post-transition metal oxides containing ns^2 lone pair state such as SnO[42] and Ba_2BiTaO_6[43].

This article aims to provide the readers an up-to-date review on aforementioned p-TCO materials. We will focus our discussions on the basic materials physics of these materials in terms of electronic structures, defect and doping chemistry for hole conductivity and optical properties.

2. Brief materials physics of TCOs

2.1 Electrical conductivity and electronic structure

The fundamentals of TCOs can be understood by the physics of semiconductors. The electrical conductivity (σ) of a TCO film is directly related to its carrier concentration (n) and carrier mobility (μ), according to the relation $\sigma = ne\mu$, where e is the elementary charge. These parameters are fundamentally related to the electronic structure of the oxides. The n is determined by the intrinsic ease of generation of mobile carriers (electrons for n-type and holes for p-type) by defects or dopants. The carrier mobility μ is directly proportional to the free carrier scattering time, τ, and is inversely proportional to the carrier effective mass, m^*, *via* $\mu = e\tau/m^*$. The τ in TCO largely depends on extrinsic factors such as ionized dopants, defects and grain boundaries determined by film preparation procedures. The m^* is an intrinsic property of the material, a tensor whose components are obtained from the electronic bandstructure by analysing the variation of energy (ε) with momentum (k). Thus, a highly dispersive valence band maximum (VBM) or conduction band minimum (CBM) gives rise to small m^* and hence a high μ.

The design strategy for state-of-the-art TCOs is to degenerately dope wide-bandgap oxide semiconductor to balance the trade-offs between n, m^* and τ. For n-type TCOs, the host materials are post-transition metal oxides (e.g., In_2O_3, SnO_2, ZnO and CdO), which usually have a large optical bandgap (> 3.1 eV) making the materials highly transparent in form of thin films. The top of VB is primarily formed by fully filled oxygen $2p^6$ states and the CBM mainly by the unoccupied ns^0 orbitals of post-transition metal cations, as depicted in Figure 1a for the case of In_2O_3. The post-transition metal ns^0 derived CBM is the key for achieving a high electrical conductivity in n-type TCOs for the following two reasons. First of all, the *ns* orbitals of post-transition metal cations normally have large spatial distributions and their

wavefunctions overlap with each other (Figure 1b), which provide a facile pathway for conduction of electrons. In the view of bandstructure, the *s* orbitals forms a highly dispersive CBM, giving rise to a small electron effective mass. Figure 1c plots the bandstructure of In_2O_3 calculated by density functional theory (DFT) by Walsh et al.[44] It clearly show a dispersive CBM at Γ point, while non-dispersive VBM. In_2O_3, ZnO and SnO_2 typically have small electron effective masses of 0.20-0.35m_e (m_e is the rest mass of an electron) and reasonably high electron mobility of 50 cm^2/Vs.[5, 20, 45] On the other hand, the effective masses for hole are as large as 38m_e for the case of In_2O_3, suggesting the fundamental limitations to obtaining highly mobile hole at the VBM. This is reflected in part by numerous attempts at p-type doping of ZnO and In_2O_3,[46-48] but no encouraging results have been achieved so far and there are still problems concerning the reproducibility of the results. Secondly owing to the d-block contraction, the energy of ns^0 of post-transition metal cations are relatively lower than those of pre-transition metals (e.g., MgO). This gives rise to a relatively high electron affinity and thus ease for doping with electrons.[49] For In_2O_3, substitution of In^{3+} by Sn^{4+} introduces dopant energy levels just below the CBM. The extra electrons can be easily activated into the CBM as free carriers, inducing a significant increase of conductivity. With more doping, the Fermi level move up into the CB and the materials ultimately show a degenerately doped semiconductor or a free electron like metallic behaviour. The critical carrier concentration n_c for the transition from an insulating to metallic phase is defined by the Mott criterion $(n_c)^{1/3} a_0^* > 0.26$, where a_0^* is Bohr radius. Taking ITO for example, literatures suggest that the static dielectric constant $\varepsilon(0) = 8.9$, an electron effective mass $m^* = 0.17m_e$, giving an effective Bohr radius $a_0^* = 2.78$ nm.[20] Thus the n_c for ITO is calculated to be 1×10^{18} cm^{-3}. For industry standard ITO, a carrier concentration of 10^{21} cm^{-3} can be achieved, together with a typically electron mobility of 50 cm^2/Vs, yielding a high conductivity of 10^4 S cm^{-1}.[5] Additionally, it should be noted that Sn dopants in the In_2O_3 lattice behave as point scatters of

the itinerant electrons and such scattering events probably set the intrinsic limits for electron mobility.

2.2 Optical properties

The optical properties of the TCO thin films are normally examined by transmittance, reflectance and absorptance spectra in a broad range of UV-visible-infrared spectrum. Their transmittance in the visible and near- infrared regions is a direct consequence of their wide optical bandgaps (E_g > 3.1 eV). Here it should be addressed that the term "optical" bandgap usually means the threshold photon energy showing strong absorption coefficient in optical absorption spectra. The "optical" bandgap is not always equivalent to fundamental (or electronic) bandgap, because some materials may have a smaller fundamental bandgap that is optically indirect or direct but excitation forbidden. Thereby the materials show very weak absorption at the fundamental bandgap. This point is very evident in the case of In_2O_3, which has an optical bandgap of 3.6 eV, yet possesses a fundamental but dipole forbidden bandgap of only 2.8 eV, see Figure 1c.[44] The fundamental bandgap is small because the large In cations lower the antibonding state at the CBM. The optical gap is substantially wider, because optical transitions between the fundamental bandgap are forbidden by the symmetry and the allowed transition is almost 1 eV below the VBM. Similarly most of the Cu^+-based delafossites p-type TCOs have fundamental bandgaps less than 2.8 eV which are indirect and show weak absorptions, but the optical bandgaps are larger than 3.1 eV.

In the near infrared region, the absorption and reflection due to the free carriers in the CB (or VB for p-type TCOs) become important. The phenomena in this region can be satisfactorily explained on the basis of classical Drude theory: the free carriers oscillate with an applied field, like the free electrons in metals (plasma oscillations). The plasmon frequency, ω_p given by:

$$\omega_p^2 = \frac{ne^2}{m^* \varepsilon(\infty)\varepsilon_0}$$

where n is the free carrier density, m^* is the electron effective mass and ε_0 is the permittivity of free space. To achieve substantial conductivity, TCOs often require carrier concentrations on the order of 1×10^{21} cm^{-3}, which results in a plasmon energy in the near-infrared region at around 0.9 eV. However a higher electron concentrations of 5×10^{21} cm^{-3} will bring the plasmon energy into the visible red spectral range. Thus the plasmon frequency for free carriers place a limit on the optimum region of transparency associated with a particular conductivity. Therefore the "transparent window" for typical TCOs is set at short wavelengths by its optical bandgap and at longer wavelengths by its reflectivity plasmon edge ($\hbar\omega_p$). Figure 2 shows transmission and reflection spectra from ultraviolet to near infrared wavelengths of an ITO films.[7] Loss in transmission at high and low wavelengths is ascribed to free carrier absorption and interband excitations.

Moreover, the additional high concentration of electrons or holes inserted into the CB (for n-type) or the VB (for p-type) can also lead to new optical transitions. As schematically shown in Figure 3a, the electrons in the CB can absorb photons and undergo transitions to higher states. Likewise, in p-type TCOs (Figure 3b), the electrons in lower states can transition up and recombine with the holes in the VB. Such second gap transitions, may affect significantly the transparency of TCOs.

2.3 Figure of merits

It is obvious the selection criteria for a high-performance TCO are of high conductivity and high transparency. From a practical point of view, these materials should also be cheap to produce, and preferably non-toxic. Researchers have been searching for a standard criterion, figure of merits (FoM), to assess the performance of materials. In 1976, Haacke[50] proposed a

simple and useful FoM that correlate the transmittance (T) and the sheet resistance R_s (where $R_s = 1/\sigma d$, d is the film thickness) by,

$FoM = T^q/R_s = T^q\sigma d$

where q is an exponent that determines which transmittance is required for a specific purpose. q = 10 is chosen because a transmittance of 90% is sufficient for most purposes. However this quantification overweighs the importance of optical transparency. A materials could have a high FoM for a transmittance >90%, even though the sheet resistance is very high (recall the q exponent). One in principle can artificially make a materials with high FoM by just making it thin enough.

The second approach with improvement proposed by Gordon[51] was to use the ratio σ/α, where α is the visible absorption coefficient. The α is calculated from the total visible transmission and corrected for reflectance (or sometime neglecting reflectance). In the neglecting reflectance approximation, $\alpha \approx (1/d)\ \ln(1/T)$ and $FoM \approx -1/(R_s \ln T)$ (in units of M Ω^{-1}). The advantage of this approach is the FoM doesn't depend on the thickness of the films, which allows more intrinsic performance of the materials to be assessed. However the functional form of this FoM means that the actual numerical values are strongly affected by changes in R_s, and are less affected by changes in T. This method seems to yield very high values for highly conductive samples, even when the optical transparency is low. For example, as shown in the following, the $Cu_xCr_{1-x}Mg_xO_2$ film is doped sufficiently high that σ is 220 S cm^{-1}, and T is 30%.[28] The FoM for this film is 4600 M Ω^{-1}, the highest values of all p-TCOs reported. However the 30% transmittance would exclude the materials a good TCO. Thus, while the FoM is a convenient parameter for the comparison of different materials from different groups, it should not be presented in isolation. It is important to look beyond the FoM and also consider σ, T, and d when evaluating p-type TCOs.

In Table I, we summarize these parameters of the representative p-type TCOs in the literature. Both FoMs by Haacke (FoM^H) and Gordon (FoM^G) are also calculated for the readers' reference. In Figure 5, we also plot the transmission *vs* inverse sheet resistance (equivalent to sheet conductance) of these p-type TCOs (red squares) and commercial n-type ITO, which provide a direct overview on the performance of p-type TCOs so far. There is still a huge gap towards the comparable performance with commercial n-type ITO.

2.4 Design rules for p-type TCOs

Lessons from n-type TCOs point out it is intrinsically a difficult task to obtain a high p-type conductivity. This is caused by (*i*) the localized nature of O 2p orbitals at the VBM (limiting the hole mobility); and (*ii*) the difficulty in p-type doping of most oxides (limiting the carrier concentration n)—in simple chemical terms, p-type doping involves the introduction of holes into the O 2p states at VBM (*i.e.*, oxidation of oxide ions); this results in strongly localized, deep lying holes centered on single oxygen sites. The key to alleviate this issue is to design a materials with cations that introduce occupied cation d or s states near the VBM. The resulting p-d and p-s coupling enhances cation-O 2p hybridization and increase the dispersion at VBM for a low effective mass. In the following we list the design principles for p-type TCOs as suggested in literature:[52-55]

Transparency: the optical bandgap must be larger than 3.1 eV to guarantee transparency to the visible light. Note also that the intraband absorption from deeper VB states to the hole states should be weak or not in visible light spectrum so as not to curtail transparency.

Hole carrier concentration: hole-producing defects (*i.e.*, acceptors) should have low formation energies, making them easy to form either as intrinsic acceptors or as extrinsic dopants soluble in the host compounds. The energy levels of the acceptors should be shallow enough so that free hole carrier can be easily activated at the VBM. "Hole-killing" defects,

such as oxygen vacancies, should be difficult to form. A review of defect formation energies of transparent oxides by Robertson and Clarke summarized the following criteria for doping[55]: for n-type doping a large electron affinity (χ, energy between the vacuum level and CBM) is necessary, while for p-type doping a small ionization potential (IP, energy difference between the vacuum level and the VBM) is required.

In the following sections, we will discuss each criterion of p-type TCOs reported in the literature based on these design rules.

3. Cu^{+}-based materials ($3d^{10}$)

3.1 Cu_2O

It is illustrative to start with Cu_2O because it is a prototype p-type metal oxide, showing a hall mobility exceeding 100 cm^2/Vs. Although its small bandgap (2.17 eV) precludes it as a p-type TCO, its electronic structure form the basic concept for designing high mobility p-type oxides. Cu_2O has a cubic crystal structure (space group $pn\bar{3}m$, a=4.27Å).[56] It consists of a body centered array of oxygen ions (see Figure 4a) with Cu ions occupying half the sites between adjacent oxygen ions, in such a way that each oxygen ion is surrounded by a tetrahedron of Cu ions and each Cu is linearly coordinated by two oxygen ions forming O-Cu-O dumbbell units. The structure can alternatively be described in terms of two interpenetrating anti-SiO_2 cristabolite nets. The separation between adjacent Cu ions in the two different nets is relatively small (3.02 Å) compared with that found in metallic copper (2.56 Å). The short Cu-Cu distance can still allow significant $3d^{10}$-$3d^{10}$ interactions, which was thought to be the cause of small bandgap of Cu_2O.[57, 58]

Cu_2O have been widely explored as one of the most promising materials for solar cells since 1920 due to their high solar spectral absorption coefficient, high mobility, low-cost, and nontoxicity.[59-61] Furthermore, due to the high p-type mobility, its applications in oxide thin

film transistors (TFT) were also extensively explored by researchers.[11, 62-64] The preparation of Cu_2O thin films has been reported using a variety of growth techniques, such as pulsed laser deposition (PLD)[63, 65, 66], magnetron sputtering[64, 67-70], thermal oxidation[71, 72], spin coating[73, 74], atomic-layer deposition[75], chemical vapor deposition[76], and so on. Among all these methods, sputtering is a relatively cost effective and the most conventional method that can be used for large area deposition of polycrystalline films, while PLD is usually used to grow epitaxial thin films on single crystal substrates.[63, 65] The obtained hall mobilities varied from largely 0.1 to 256 cm^2/Vs. Li *et al.* achieved a record mobility of 256 cm^2/Vs in Cu_2O polycrystalline thin films by introducing a low-temperature buffer Cu_2O layer to control the preferential crystalline orientation and increase the grain size.[67] An increasing Hall mobility was found with larger grain sizes, indicating that grain-boundary scattering is a major contributor in limiting the electrical properties. Matsuzaki and co-workers have grown Cu_2O epitaxial thin films on both MgO(001) and (110) substrates and their films possess a hole mobility of up to 90 cm^2/Vs at room temperatures.[63] Interestingly, the hole mobility increased up to μ=363 cm^2/Vs as temperature decreased to 170 K. The authors also fabricated p-channel thin film transistors using the Cu_2O films. However the device only exhibited a low field-effect mobility at 0.26 cm^2/Vs, regardless of the high phase purity and Hall mobility of the thin films they achieved. This result implied possible extra trap states at the channel and/or channel-gate interface produced during device fabrication process, e.g., by ion bombardment and/or plasma reduction, may play an important role in determining the device performance.[77] This is also true for application of Cu_2O in solar cells. It has been demonstrated the formation of interfacial defect states (possibly CuO) between the heterojunction of p-Cu_2O and n-ZnO is detrimental to the efficiency of Cu_2O-based solar cells.[78-80] Therefore controlling the surface and interface chemistry of Cu_2O thin films with other materials might be the solution to address the problem.

The higher p-type mobility of Cu_2O is related to nature of the bandstructure near the top of VB. The VB of most metal oxides are mainly composed of O 2p orbitals, leading p-type doping to often result in localized holes deep in the bandgap. In contrast, Cu^+ in Cu_2O has $3d^{10}$ close shell electronic configuration. The energy level of Cu $3d^{10}$ is close to that of O $2p^6$ orbitals (Figure 4b). This leads to a considerable covalency between the two orbitals. In such a way, a more dispersed VBM with a smaller hole effective mass can be achieved. Photoelectron spectroscopy measurements and bandstructure calculations clearly show that the Cu 3d levels and the O 2p states are close in energy and that these form the top of VB.[81, 82] Figure 4c show the bandstructure of Cu_2O calculated by Nie *et al.* using DFT -local density approximation (LDA).[83] It clearly shows that the VBM at Γ point is much more dispersive than that of In_2O_3 (Figure 1c). By analysing the variation of energy (ε) with momentum (k), the authors also report a hole effective mass as low as $0.24m_e$. This value is slightly smaller than the experimental data ($0.58m_e$ and $0.69m_e$) measured by cyclotron resonance,[84] due to the underestimation of the bandgap by LDA. DFT has a well-known tendency to underestimate bandgaps in most semiconductors and insulators. This tendency is due mainly to a discontinuity in the exchange correlation potential. Nonetheless, these results provide microscopic mechanism for the p-type high mobility found in Cu_2O.

It is now widely accepted that the source of p-type carriers in Cu_2O is Cu vacancies (V_{cu}), *via*, $V_{cu} \rightarrow Cu^{(0)} + h^{\bullet}$ (the formation of a V_{cu} is associated with removal of one Cu atom from the lattice, together with one hole state above the VBM).[85-87] This is supported by accumulative experimental observations that the hole concentration in Cu_2O are strongly correlated with oxygen partial pressure during growth or post-growth annealing conditions in oxygen.[56, 67] A direct evidence of V_{cu} has been reported by F. Ameena *et al.* by using positron annihilation spectroscopy (PALS) in conjunction with Doppler broadening spectroscopy (DBS) and photoluminescence (PL) spectroscopy.[88] Theoretical studies based on different

methods (LDA, GGA+U) also consistently predicted V_{cu} has the lowest formation energy compared to the other possible defects (e.g., oxygen interstitial) both under Cu-poor-O-rich condition, and under Cu-rich-O-poor condition.[83, 86, 89, 90]

It is still quite debated in literature on the energy level of the hole state (*i.e.*, acceptor levels). The hole state have been reported in experiments in the range of 0.12–0.70 eV above the VBM.[65, 90-93] Based on the elementary effective mass theory, the acceptor energy can be roughly estimated by $E_A=13.6m^*/m_o\varepsilon_r^2$. One obtains a hole energy level of 0.156 eV above VBM. This is of course an oversimplified estimation, because unlike conventional semiconductors of covalent bonding, Cu_2O is an ionic compound in which the charge carrier favours to form self-trapped polarons by distorting the surrounding lattice.[90] The polaronic nature of the carrier would result in much deeper acceptor levels trapped in the bandgap. Deep acceptor states were observed with photoinduced current transient spectroscopy, with the defect states having activation energies ranging 0.12–0.63 eV above the VBM.[91] The acceptor state at 0.63 eV was assigned as V_{cu} acceptor-type state. None of the other defect levels were assigned. Paul *et al.* recently performed a detailed study on the defects of Cu_2O using deep level transient spectroscopy with a broad temperature range of 100 to 350 K, and reported two hole trap levels.[92, 93] The first at 0.45 eV above the VBM, similar to the ones found by others,[91] was attributed to V_{cu}, while the second level located at 0.25 eV was tentatively assigned to a Cu di-vacancy. Scanlon and Watson *et al.* have calculated the energetics and the transition levels of acceptor defects in Cu_2O using hybrid-DFT approach.[86, 90] They successfully predicted the two transition levels, one at 0.47 eV and the other at 0.22 eV, in excellent agreement with the DLTS study by Paul *et al.* and others.[92, 93] Their results were also consistent with the polaron hopping transport mechanism as experimentally observed Arrhenius-like temperature dependence conductivity.[64, 94]

3.2 Delafossite (Cu*M*O_2)

3.2.1 Crystal structures and thin film growth

However, for all reported Cu_2O thin films, despite the encouraging hall mobility values, a major concern is the low carrier concentration (ca.10^{14} cm^{-3}) and low optical bandgap (ca. 2.17 eV), which limit the potential of Cu_2O thin films in fully transparent electronics. The small bandgap of Cu_2O was believed to be due to the strong Cu-Cu interaction in a cuprite structure: each Cu ion has 12 next-nearest Cu^+ neighbours.[27, 58] It was therefore suggested that a large bandgap might be found in ternary Cu^+ Hosono and co-workers found thin films of $CuAlO_2$ have a large optical bandgap of 3.5 eV and therefor show simultaneously an optical transparency of 70% and p-type conductivity of 1 $S.cm^{-1}$.[25] Figure 6 show the optical transmission spectra and temperature dependent conductivity measurement of $CuAlO_2$ thin film, originally reported in ref. [27]. This pioneering work has aroused intense interest for search for other Cu^+-based delafossites with the general chemical formula $CuMO_2$ in which *M* is trivalent cations such as B, Al, Cr, Ga, Sc, In and Y. In the delafossite structure (Figure 7a), each Cu atom is linearly coordinated with two oxygen atoms, forming O-Cu-O dumbbells parallel to the c axis. The oxygen anions in the O-Cu-O dumbbells are also each coordinated to three M^{3+} cations, oriented such that *M*-centered octahedral form MO_2 layers which lie parallel to the *ab* plane. The O-Cu-O dumbbell and the octahedral MO_2 can be arranged in layers so that a stacking sequence of *ABABAB* gives the 2H (P63/mmc) hexagonal polymorph or *ABCABC* gives the 3R ($R\bar{3}m$) rhombohedral polymorph.

Table II summarize the structural parameters of the undoped $CuMO_2$ ($R\bar{3}m$) which were retrieved mostly from powder ceramics prepared by solid state synthesis back in 1980s.[95-97] It can be seen that the lattice parameters and bond lengths follow well the trend of ionic radius of M^{3+}. The local coordination around Cu^+ in $CuMO_2$ is very similar to that in Cu_2O, *i.e.* the same O-Cu-O dumbbells and similar Cu-O bond distance. The most important difference between the two oxides is that the O-Cu-O units in Cu_2O are connected in three dimensions,

whereas in CuMO_2 the O-Cu-O units are isolated by the MO_2 layers into two-dimension. Therefore the number of next-nearest-neighbours is reduced from 12 in Cu_2O to 6 in CuMO_2. It has been argued that the reduced dimensionality of the Cu-Cu interactions is of central importance in determining that the bandgap of $CuAlO_2$ (originally quoted as 3.5 eV) is wider than that in Cu_2O (2.17 eV).[25, 27] However, there is oversimplified picture, because one should note that the Cu-Cu bond distance in CuMO_2 (2.86 Å) is shorter than that of Cu_2O (3.02 Å).[58, 98]

Since the seminal work of $CuAlO_2$, considerable efforts have been made to grow a variety of CuMO_2 (M = B[99, 100], Al[25, 27], Cr[28], Ga[33], Sc[31, 101], In[30, 102] and Y[32]) and their alio-valent cation doped thin films (*e.g.*, Mg doped $CuCrO_2$, Mg doped $CuAlO_2$) by techniques such as PLD,[25, 27, 30, 33101] sputtering,[28, 31, 32, 102, 103] molecular beam epitaxy,[104] chemical solution methods,[105-107] and so on (see ref. [24] for a comprehensive review on the p-type TCO deposited by different techniques). PLD is the most popular growth method because it has the advantage of growing high-quality epitaxial thin films with well-controlled compositions and morphology. The epitaxial growth of CuMO_2 film with reduced defects and grain boundaries would be desirable for (opto-)electronic device application (*e.g.*, transparent p-n diodes) as well as for fundamental research to study the intrinsic properties of the materials. However preparing a high-quality CuMO_2 ceramic target is challenging because of the metastable oxidation state of Cu^+ and the ease to form secondary phase.[108] Basal plane alumina Al_2O_3(0001) was the most popular substrate for attempted epitaxial growth of CuMO_2 films, and silica substrate were also used for polycrystalline films. The structure of alumina belongs to the rhombohedral space group $R\bar{3}c$. It is based on a hexagonally close packed array of oxygen ions with occupation of 2/3 of the octahedral holes between successive layers by aluminium ions. The average O-O separation in the close packed layers is $d_{O-O} = a_{Al2O3}/\sqrt{3} =$ 2.748 Å . It is thus expected the CuMO_2 can be epitaxially grown on

the Al_2O_3(0001) by matching of both the crystal symmetry and the nearest-neighbour O–O distances. For example, the in-plane lattice parameter and also the d_{O-O} of $CuAlO_2$ are 2.858 Å; and thus the mismatch between $CuAlO_2$ and Al_2O_3 can be defined by $f = (2.858 - 2.748)/2.748 = 4.0\%$, with $CuAlO_2$ under compressive strain. It has been shown the c axis of $CuAlO_2$ is parallel to that of Al_2O_3 substrate, and the in-plane axes rotate 60° around the c axis to keep the close-packed stack of oxygen ions at the interface of between $CuAlO_2$ and Al_2O_3.[109] Similar epitaxial relationship have been observed for $CuBO_2$[99], $CuCrO_2$[104] and $CuGaO_2$[33, 107]. However, with the increase of the ionic size of *M* cations, the lattice mismatch is too large to maintain the epitaxial relationship (*e.g.*, f = 19.8% for the case of $CuInO_2$). H. Yanagi *et al.* found the growth of Ca- and Sn- doped $CuInO_2$ on Al_2O_3(001) leads to polycrystalline films.[30]

3.2.2 Electronic and optical properties

The optical and electrical properties of the films were commonly evaluated by UV-visible absorption, temperature dependent conductivity measurement, Hall and Seebeck coefficient measurement, and the results are summarized in Table I and Figure 5. Compared to Cu_2O, Cu-based delafossites normally have higher conductivity and transparency, but lower hole mobility (< 10.4 cm^2/Vs). Sleight and co-workers suggested the lower mobility in the p-type delafossites may be due to the lack of three dimensional Cu–O–Cu linkages as seen in Cu_2O, while in the delafossite structure there are only Cu–O– *M*–O–Cu linkages.[110] This statement is supported by later report that the electrical conductivity along ab plane of $CuAlO_2$ single crystal is 25 times higher than that along the c axis.[111] Similar anisotropic ratio (~30 times) has also been reported for $CuCrO_2$ single crystals.[112] Scanlon and Watson *et al.* calculated the electronic structures and effective masses of Cu*M*O_2 (M=Al, Cr, Sc and Y) using DFT corrected for on-site Coulombic interactions (GGA+U) which gives a more accurate bandgap values than GGA and LDA.[113-115] Their results show $CuAlO_2$ have an effective mass of $2.6m_e$

in ab plane, while a large effective mass of 38.95m_e along the c axis. Similar anisotropy in effective masses have also been obtained for $CuBO_2$,[116] $CuCrO_2$,[114] $CuScO_2$[115] and $CuYO_2$[115], as summarized in Table II. It is also of interest to discuss the effect of M^{3+} cation on the trend of effective masses. As the sizes of the M^{3+} cations increase, the Cu-Cu distance (equal to the *ab* lattice constant) increase. The larger Cu-Cu distance reduces the dispersion at VBM and hence results in a higher effective masses. Overall all the CuMO_2 have much larger effective masses than that of Cu_2O (0.58m_e determined by experiment[84] and 0.24m_e by LDA calculation[83]), which might explain much lower motilities commonly observed in CuMO_2.

Considering $\sigma=en\mu$, the higher conductivity in delafossites compared to Cu_2O should be associated with the a higher hole concentrations produced by a higher density of native acceptor-like defects *(e.g., V_{cu})* and/or intentional divalent doping at M^{3+} sites. Divalent doping (*e.g.*, Mg^{2+}) is a straightforward way to introduce hole carriers. Provided the oxygen stoichiometry is unchanged, each divalent cation substituting at M^{3+} site should in principle introduce one hole state. $CuAl_{1-x}Mg_xO_2$[27], $CuCr_{1-x}Mg_xO_2$[28], $CuSc_{1-x}Ca_xO_2$[28], $CuIn_{1-x}Ca_xO_2$[30] and $CuY_{1-x}Ca_xO_2$[32] with $0<x<0.05$ have been reported showing higher conductivities than their undoped forms. Attempt has been made for doping $CuGaO_2$ with Mg, but was not successful.[33] To date $CuCr_{0.95}Mg_{0.05}O_2$ polycrystalline films reported by Nagarajan *et al.* in 2001 has the record highest conductivity (220 S/cm) of any p-type TCOs, but the films only have 30-40% transmittance.[28] The electronic structure of $CuCrO_2$ has been found to be very similar to that of other Cu^+-based oxides: Cu $3d^{10}$ intermix strongly with O $2p^6$ to form the top of VB .[29, 114, 117] The role of Cr 3d states has been a matter of debate, because it is experimentally difficult to pinpoint the energy position of Cr 3d state. [29, 105, 118] A recent study based on resonant PES, X-ray absorption (XAS) and DFT calculations by Yokobori and co-workers suggest that the Cr 3d states straddle most of the top of VB and hybridize strongly with Cu 3d and O 2p states.[119] The significant Cr 3d contribution at the top of VB

suggests that the holes introduced into $CuCrO_2$ by p-type doping are partially delocalized onto Cr.[118, 119] This possibly accounts for the higher conductivity of $CuCrO_2$ as compared with $CuAlO_2$. Meanwhile Cr^{3+} cations at oxygen octahedrons also show d-d excitations with an energy of 2.6 eV which may explain the low transparency of $CuCrO_2$. [28, 104]

$CuInO_2$ is another materials of particular interest, because it is amenable to bipolar doping, where p- or n-type doping can be achieved by Ca or Sn substitution, respectively.[30, 120] The bipolar dopability of $CuInO_2$ can be understood within the framework of equilibrium doping theory. According to the "doping limit rule" reported by Zhang *et al.*, a compound with higher VBM is easier to dope p type, while a compound with lower CBM is easier to dope n type.[120] LDA calculations indicate that the VBM of $CuInO_2$ is mainly composed of Cu $3d^{10}$ with some mixture of O 2p state, therefore explaining the p-type dopability. The CBM is mainly formed by low lying In 5s state in a similar way as the case for In_2O_3, which explain the n-type dupability by Sn. However no much attempt has been made to bipolar doping of $CuInO_2$ after ref [30].[121] It would be interesting to re-investigate this system based on high-quality thin films.

For nominally "undoped" Cu*M*O_2, V_{cu}, oxygen interstitials (O_i) and antisite (Cu_M) are believed to be the possible source of hole carriers. Perllicer-Porres *et al.*[122] and Tate *et al.*[111] postulated that V_{cu} is the dominant native defects responsible for the p-type conductivity in $CuAlO_2$ based on optical absorption spectra of high-quality $CuAlO_2$ single crystals. This is supported by DFT calculations by Katayama-Yoshida et al.[123, 124] and Nolan[89] who report V_{cu} has the smallest formation energy. However, recently Scanlon and Watson using more advanced hybrid-DFT have shown that besides V_{cu}, Cu_{Al} antisites are also dominant defects under Cu-poor/Al-poor conditions.[113] Their calculations also found the transition levels of these defects are deep in the bandgap being at 0.68 eV above VBM, in agreement with the experimental value (0.70 eV) deduced from optical absorption.[111] Interestingly, as the size of

M^{3+} cation increase (*e.g.*, $CuYO_2$ and $CuScO_2$), O_i become more energetically favourable because of the more open lattice structure to accommodate excess oxygens.[31, 125] One O_i can trap two electrons leaving behind two hole states at the VB ($O_2(g) = 2O_i'' + 4h^{\bullet}$). It has been shown that $CuScO_{2+x}$ and $CuYO_{2+x}$ can intercalate excess oxygen up to x>0.5 by annealing the materials in oxygen-rich conditions, while there is negligible excess oxygen detected in $CuAlO_{2+x}$ (x<0.00002).[98, 125] Duan *et al.* prepared $CuScO_2$ polycrystalline thin films on silica by sputtering and found the as-prepared films were insulating.[31] Treating the films under oxygen at 450 ^oC significantly increased the conductivity up to 30 S cm^{-1}, the highest conductivity reported for nominally "undoped" Cu*M*O_2. They suggest O_i was dominant defects for p-type carrier in $CuScO_{2+x}$.

3.2.3 $SrCu_2O_2$

$SrCu_2O_2$ does not possess a delafossite structure but can be viewed as an extension of Cu-based delafossite. As shown in Figure 8a, $SrCu_2O_2$ crystallises in a tetragonal structure with a unit cell of a = 5.480 Å and c = 9.825 Å. This crystal has the same O-Cu-O dumbbell zigzag chains separated by SrO_6 octahedron. It is therefore expected that reduction of dimension also leads to a large bandgap relative to Cu_2O, similar to that of Cu delafossite. Kuo *et al.* prepared both undoped and 3% K doped $SrCu_2O_2$ thin films by PLD.[34] The undoped film show a low p-type conductivity of $3.9x10^{-3}$ S cm^{-1} and mobility of 0.46 cm^2/Vs. The conductivity could be slightly increased to $4.8x10^{-2}$ S cm^{-1} by 3% K doping, but the carrier concentration are still three orders of magnitude less than K doping concentration.

The electronic structure of $SrCu_2O_2$ have been examined by photoelectron, optical spectroscopy and DFT calculations.[83, 126, 127] The VBM is formed by the antibonding state of Cu 3d with O 2p, while the CBM is primarily composed of Cu 4s (Figure 8b).[128] Godinho et al. have performed GGA and GGA+U calculations on the electronic structure and defects of $SrCu_2O_2$.[129, 130] They found the lowest hole effective masses (0.78 m_e) is along the [100] and

[010] directions, *i.e.*, the zigzag O-Cu-O dumbbell chain direction. Their results also suggest V_{cu} and Sr vacancies (V_{Sr}) are the most likely native defects leading to p-type conductivity in undoped films.

Optical measurements indicated that $SrCu_2O_2$ is a direct bandgap materials (E_g=3.3 eV).[126] This is in contrast to the case for delafossites where an indirect bandgap normally appear at visible light region. A direct bandgap semiconductor is highly desirable for many optoelectronic devices such as light-emitting diode (LED) and laser diodes. In addition, $SrCu_2O_2$ thin films can be deposited at temperatures as low as 350°C, making it possible to minimize the chemical reaction. Thereafter $SrCu_2O_2$ have received much attention used as an active p-type semiconductor in combination with available n-type oxides to form p-n heterojunctions. Kudo et.al. have fabricated all oxide-based transparent p-n heterojunctions composed of n^+-ZnO/n-ZnO/p-SCO/ITO deposited on glass substrates where the n^+-ZnO and ITO are used as transparent electrodes, as shown in Figure 8c and d.[131] The diode had an average transmission of ≥ 70% in the visible spectrum (Figure 7d). A typical current voltage (I-V) characteristic of the p-n heterojunction diode. Ohta *et al.* have successfully fabricated an ultraviolet LED by epitaxially growing p-$SrCu_2O_2$ on n-ZnO by PLD.[132] Their p-n heterojunctions emit a sharp emission band centred at 382 nm at room temperature, which demonstrate $SrCu_2O_2$ can be used as an optically active p-TCO material for optoelectronic devices.

4. Layered oxychalcogenides

These Cu^+-based ternary p-type transparent oxides still suffered from low hole concentration and low carrier mobility. As a consequence, the CMVB was also extended by using chalcogen (Ch= S, Se, and Te) elements p orbitals to replace the oxygen ones, since a more dispersed VBM was theoretically expected from stronger hybridization between Cu 3d and Ch p orbitals, due to the increasing covalency between Cu and Ch atoms in the sequence of

O, S, Se, and Te. Following this concept, the first materials being identified as a p-TCO was LaCuOS layered oxysulfide by Hosono and co-workers in 2000,[36] although the crystal structure and p-type conductivity of this materials have been reported by many other researchers.[133] The crystal structure of LaCuOS is composed of CuS and LaO layers alternately stacked along the c axis (Figure 9a).[133, 134] In the CuS layers, Cu is tetrahedrally coordinated by four S ions, forming the upper part of the VB and conduction paths for holes; the LaO layers confine the CuS in two-dimensional layers, leading to a large bandgap of 3.1 eV.[135] Therefore LaCuOS is transparent in the visible region. The conductivity can be controlled over a wide range by substitution of La^{3+} by divalent Sr^{2+} or Mg^{2+}, in a similar way to the well-known hole-doped perovskite transition metal oxides.[136] It has been demonstrated by Hiramatsu *et al.* that the hole concentrations and conductivities can be increased from 2×10^{15} cm^{-3} and 0.00006 S cm^{-1}, up to 2.7×10^{20} cm^{-3} and 20 S cm^{-1} respectively, by doping LaCuOS with 3% Sr at La sites (Figure 9b).[137, 138] The hole concentration obtained in this result is extremely high among the p-type TCOs reported. Interestingly temperature dependence of conductivity measurement (Figure 9b) indicate the 3% Sr doped film exhibit a degenerately doped semiconductor conduction mechanism, and thus offer promising potential for development of a high performance p-TCO to rival their n-type counterparts.

In addition to these wide-gap and conducting properties, photoluminescence spectra study also indicated LaCuOS has a direct allowed bandgap.[37, 135] Due to its large exciton binding energy (~59 meV), LaCuOS emits UV light associated with excitons at room temperature, which makes LaCuOS a unique materials similar to ZnO but of p-type character. This notable property offers promise as an active layer in optoelectronic applications such as UV or vilolet LEDs.[12, 139]

Furthermore, the bandgap of LnOCuCh can be largely tuned by controlling the chemical compositions at Ch sites.[140] The bandgaps decrease from 3.1 eV for LaOCuS, 2.82 eV for LaOCuSe and 2.31 eV for LaOCuTe.[141, 142] The chemical trend of the bandgaps can be simply understood from the decrease of the energy levels of Ch np^6 orbitals (S>Se>Te): Ch np^6 form the top of the VB with Cu $3d^{10}$ orbital. Hosono and co-workers have prepared $LaCuOS_{1-x}Se_x$ (x=0, 0.25, 0.50, 0.75, 1.0) solid solutions in form of polycrystalline bulk and epitaxial thin films, and found their bandgaps change almost linearly from 3.1 eV to 2.8 eV as x varies from 0 to 1.[38, 143] The hall mobility increases as x and reaches 8.0 cm^2/Vs in LaCuOSe. A remarkably high hole density of 1.7×10^{21} cm^{-3} and a room temperature conductivity of 910 S cm^{-1} has been achieved on Mg-doped LaCuOSe epitaxial films.[144] Unfortunately this materials shows low transmittance for visible light because of the smaller bandgap of LaCuOSe (2.8 eV) and absorption arising from in-gap hole states, making it not suitable as a p-TCO.

Recently, Liu et al. have synthesized $Sr_3Cu_2Sc_2O_5S_2$ polycrystalline bulks as a p-type TCOs.[40] Its structure also belongs to layered oxysulfide, composed of similar two dimensional CuS slabs confined by perovskite-like $Sr_3Sc_2O_5$. The authors showed this material has a wide energy gap of 3.1 eV (but also with strong absorption at lower energy), an intrinsic p-type conductivity of 2.8 S cm^{-1} and a remarkable high mobility of 150 cm^2/Vs, even higher than the highest mobility reported for n-type TCO. Scanlon *et al.* have performed GGA+U and HSE06 calculations on the electronic structure of $Sr_3Cu_2Sc_2O_5S_2$.[145] Their results suggests this materials has a direct optical band gap of ~3.5 eV. Detailed analysis of the bandstructure indicated a strong mixing of the S 3p states and the Cu 3d states at the VBM is the cause of the high mobility in agreement with the experimental result by Liu *et al*. It is undoubtedly of significant interest to prepare this materials into thin films and dope it

with monovalent cations (K^+) at Sr sites or divalent (Mg^{2+}) at Sc sites to improve the conductivity in this materials.

5. Spinel oxides (nd^6)

The essence of chemical design concept is to modulate the top of the VB by intermixing oxygen $2p^6$ with closed shell Cu $3d^{10}$ orbitals to reduce localization of holes in oxygen ions and meanwhile avoid colorization from metal d–d excitation. This concept also leads to the idea that transition metal ions (Co^{3+}, Rh^{3+} and Ir^{3+}) with a d^6 configuration in an octahedral oxygen coordination may behave similarly to Cu $3d^{10}$, since their low spin ground states could be regarded as a "quasi-closed" shell configuration. As shown in Figure 10b, the d orbital is the octahedral ligand field splits d orbital into sixfold degenerate t_{2g} and fourfold degenerate e_g states. The t_{2g} states are fully occupied by all six electrons with low spin configuration forming the top of VB, while the empty e_g states forms CBM. Following this concept, a new class of non-d^{10} p-TCO, ZnM_2O_4 (M = Co, Rh, and Ir) were identified.[41, 146] ZnM_2O_4 have a normal spinel crystal structure (Figure 10a) with Zn occupying the tetrahedral sites and M occupying the octahedral sites. Mizoguchi et al. first reported $ZnRh_2O_4$ thin film exhibited p-type TCO behaviour with an electrical conductivity of 0.7 S cm^{-1} with no intentional doping and a bandgap of 2.1 eV.[147] The authors also confirmed that the electronic configuration of Rh $4d^6$ was in the low spin state of $t_{2g}^6\, e_g^0$ by magnetic susceptibility measurement and the bandgap is indeed defined by the fully filled t_{2g}^6 state hybridizing with some O 2p (VB) and empty e_g^0 orbital (CB) using photoemission spectroscopy. Despite of the small bangap of 2.1eV, $ZnRh_2O_4$ show transparency to visible light because the bandgap is of d-d character whose transition is dipole forbidden. Unlike Cu-delafossites where the O-Cu-O dumbbell are confined in two-dimensional, the RhO_6 octahedra in $ZnRh_2O_6$ are tightly connected through edge-sharing into a three dimensional structure. This enhances the hybridization between metal d and O 2p orbitals, and thus the hole conduction path is three-

dimensional. As a consequence, it has been demonstrated that the amorphous $ZnRh_2O_4$ thin films retain its p-type character when used in a p-n diode based on amorphous $ZnRh_2O_4$ on amorphous n-type $InGaZnO_4$.[146] The p-type conduction in the amorphous structure might originate from the isotropic nature of the spinel structure and the edge-sharing RhO_6 networks, which are less affected by the structural disorder and are even stable in an amorphous network.

After the pioneering of $ZnRh_2O_4$, Dekkers *et al.* reported the growth of p-type $ZnCo_2O_4$, $ZnRh_2O_4$ and $ZnIr_2O_4$ polycrystalline and epitaxial thin films by PLD.[41] Conductivities of 0.39 S cm^{-1}(0.61 S cm^{-1}), 2.75 S cm^{-1}(2.83 S cm^{-1}) and 3.39 S cm^{-1}(2.09 S cm^{-1}) are obtained for polycrystaline (epitaxial) films of $ZnCo_2O_4$, $ZnRh_2O_4$, and $ZnIr_2O_4$, respectively. Based on optical absorption spectra, the authors also showed the bandgaps of $ZnCo_2O_4$, $ZnRh_2O_4$, and $ZnIr_2O_4$ are 2.26 eV, 2.74 eV, and 2.97 eV. The increase of bandgaps (Co<Rh<Ir) is argued due to the increasing crystal field splitting between t_{2g} and e_g in going from 3d(Co)<4d (Rh)<5d (Ir). However, the magnitude and trend of bandgaps reported by Dekkers are at variation with other experiments and theoretical works. For example, the bandgap of $ZnRh_2O_4$ has been measured to be 2.1 eV by Mansourian-Hadavi *et al.*[148] and 1.2 eV by Sing *et al.*[149], while the values from DFT dependent on calculation methods range from 0.8 eV to 3.2 eV.[150, 151] A re-investigation of the optical and electronic structure of these materials based on high-quality thin films is thus needed to resolve these fundamental issues.

$ZnCo_2O_4$ is probably the most studied of ZnM_2O_4 spinels, with much interest generated due to its possible applications in photo-(electro-)catalysis[152-154], supercapacitors[155] and Li ion batteries[156, 157]. Kim *et al.* reported $ZnCo_2O_4$ has an optical band gap of 2.63 eV, and can show both p-type (a conductivity of up to 21 S cm^{-1}) and n-type conductivity by controlling the oxygen pressure.[158] Recently, Grundmann and co-workers demonstrated amorphous p–n

junction diodes and field-effect transistors using p-type $ZnCo_2O_4$ deposited at room temperature, indicating potential of this material for oxide electronic applications.[159-161]

There is general consensus the intrinsic p-type conductivity of ZnM_2O_4 originated from the acceptor-like antisite defects Zn_M and/or Zn vacancy (V_{Zn}).[150, 151] DFT calculations also found no significant dispersion in VBM and a large hole effective masses. Perkins *et al.* found a hole effective mass of $18m_e$ for $ZnCo_2O_4$ and this a small mobility of 0.028 cm^2/Vs by combining DFT calculations and experimental measurements on polycrystalline sample.[162] The polaronic conduction mechanism generally found on ZnM_2O_4 may be the limiting factor for high electrical conductivity. The high price of precious Rh and Ir metal also constraint their large-scale production for industrial applications.

6. Cr-based oxides ($3d^3$)

Continuing with the idea of quasi-closed shell, Cr^{3+} with a d^3 in an octahedral oxygen coordination should give a similar electronic configuration at the VBM as d^6 and d^{10} materials. The oxygen octahedral field splits Cr 3*d* orbitals into an occupied t_{2g}^3 level forming the top of the VB, and an empty $t2g^0$ and two empty e_g^0 levels forming the bottom of the CB. Cr_2O_3 and $LaCrO_3$ are two Cr-based oxide identified as potential p-type TCO.[163, 164] Cr_2O_3, also known as chromia (mineral name Eskolaite), crystallizes in the corundum structure with hexagonal closed packed layers of oxygen atoms and two-thirds of the octahedral sites filled with Cr atoms. The optical bandgap of Cr_2O_3 is reported to be 3.4 eV, arising from the strong excitation from O 2p to Cr t_{2g} and e_g.[165, 166] Below this strong absorption, Cr_2O_3 also shows two weak absorptions at 2.0 eV and 2.6 eV, which are usually attributed to dipole forbidden d−d transition from occupied t_{2g} to empty e_g levels and is responsible for the green color of Cr_2O_3 powders but are weak enough not to reduce the transparency of the material in form of thin film. Stoichiometric Cr_2O_3 is usually highly insulating, although there are reports of very low native p-type conductivity arising from Cr vacancies. N. Uekawa and K. Kaneko have

reported doping Cr_2O_3 polycrystalline with Li^+, Mg^{2+}, Ni^{2+} *etc.* at Cr site can enhance the p-type conductivity by introducing hole state at the top of VB, *i.e.,* at the Cr 3d t_{2g}.[167] E. Arca *et al.* was the first who demonstrated the use of Cr_2O_3 thin films as a p-type TCOs.[163] They found Mg and N co-doped Cr_2O_3 produced a p-type oxide with conductivity of 0.33 S cm^{-1} and transmission up to 65% for a 150 nm thick film. A detailed analysis on epitaxial Mg:Cr_2O_3 films grown on Al_2O_3 by the same group showed a small polaron hopping conduction being the limiting factor in the material's conductivity.[168, 169]

Recently Zhang et al. have reported perovskite Sr-doped $LaCrO_3$ ($La_{1-x}Sr_xCrO_3$) with high figure of merits as new p-type TCOs.[164] The authors have shown that the lowest excitation in $LaCrO_3$ results from a $t_{2g}^3 \rightarrow e_g^0$ transition is at ≈2.8 eV but formally dipole forbidden. The strongest optical absorption resulting from O 2p to Cr e_g^0 falls at ≈4.6 eV, which makes undoped $LaCrO_3$ highly transparent but insulating.[170] Substituting Sr^{2+} for La^{3+} in LCO effectively dopes holes into the top of the VB and results in p-type conductivity (Figure 11b and c).[171] The perovskite structure represents an advantage for this materials, because it allows one more easily to dope it and integrate with the workhorse of other perovskite oxides which exhibit interesting properties such as high superconducting temperature superconductors, colossal magnetoresistance and ferroelectricity.[136] It has been shown the p-type $LaCrO_3$ films can form isostructural and coherent interface with the well-known n-type $SrTiO_3$, see Figure 11a. XPS reveals that the $LaCrO_3$/$SrTiO_3$ heterojunction exhibits a type-II staggered band alignment.[172] In contrast, the transparent p–n junctions fabricated using p-type Cu*M*O_2delafossites and n-type ZnO form much more defective interfaces because of their very different crystal symmetries. These considerations have implications for the fabrication of all-perovskite oxide transparent electronic devices.

7. Lone pair based oxides (ns^2)

The chemistry of post transition metals is dominated by the group oxidation state N and a lower N-2 oxidation state. The N-2 state is associated with occupation of a metal cation ns^2 lone pair (*e.g.,* Sn^{2+} and Bi^{3+}). The ns^2 lone pair can interact strongly with O 2p by distorting the lattice, forming antibonding states at the top of VB.[173-175] Because cation s orbitals are generally more spatially extended than d states, and it is therefore expected their hybridization with O 2p states can result in lighter effective mass (in a way similar to the case of n-type TCOs). SnO (Sn^{2+}: $5s^2$) is one of the materials that has been receiving considerable attentions as a p-type semiconductor.[11, 42, 176-179] The stable phase of SnO adopts a layered tetragonal structure (litharge), space group P4/nmm, with each Sn atom positioned at the apex of a square pyramid formed by four oxygen atoms (Figure 12a). The Sn and O atoms arranged alternatively with layered structure in a $Sn_{1/2}$–O–$Sn_{1/2}$ layer sequence. The lone-pair Sn $5s^2$ is projected out into the void space between the $Sn_{1/2}$ layers along the [001] crystallographic direction. The formation of a distortion in the lattice allows significant mixing between Sn 5s and O 2p states, giving rise to a filled antibonding state with some 5s character at the top of the VB.[180, 181] This situation is clearly manifested in the bandstructure of SnO calculated by DFT, showing a dispersive VBM at Γ-point, and interestingly dispersive CBM at M point (Figure 12).[39, 180, 181] The dispersive CBM can be understood the low lying Sn 5p state hybridized with Sn 5s. Therefore the DFT calculations reveal that SnO has an "indirect" fundamental bandgap of 0.61 eV between the Γ- and M-points. The direct bandgap with strong optical absorption is reported to be between 2.6-3.2 eV, which explains the reasonable transparency of SnO.

The interest in SnO was sparked by Ogo and co-workers who grew SnO epitaxial films on yttira-stabilized zirconia (YSZ) substrates by PLD in 2008, showing a Hall mobility of 2.4 cm^2/Vs and a field-effect mobility of 1.3 cm^2/Vs when used as a p-channel TFT. Subsequently both epitaxial and polycrystalline thin films have been fabricated several

groups using a variety of technique such as PLD, sputtering and e-beam evaporation.[11, 42, 176-179] All the results show SnO thin films have intrinsic p-type conductivity with a Hall mobility around 1-5 cm^2/Vs. Furthermore, Hosono et al. have shown n-type SnO can be achieved by Sb doping with a mobility of 2 cm^2/Vs, which makes SnO as a promising bipolar conductor for n- and p-type TFTs and p-n junctions.[177, 182] However the issue with SnO is that SnO is very unstable and can be easily either over-oxidized into SnO_2 or reduced into metallic Sn. It is still challenging to deposit a single-phase thin film. Even so, controlling its surface/interface represent another challenge for device fabrication.

Ba_2BiTaO_6 is another interesting novel p-TCOs taking advantage of Bi $6s^2$ lone pair state, which has been recently identified through a high-throughput computational screening methodology by G. Hautier and co-workers.[26, 43] Ba_2BiTaO_6 has a rhombohedral double perovskite structure, containing an ordered array of Bi^{3+} and Ta^{5+} ("B-site") octahedral surrounded by Ba^{2+} ("A-site"). Their calculations show that the Bi^{3+} with filled $6s^2$ orbitals hybridizes strongly with O 2p, increasing the extent of the dispersion at VBM and effectively reducing the valence effective mass, while Ta^{5+} forms a CBM with low electronegativity, leading to a large bandgap (> 3.8 eV) for optical transparency. The authors also synthesized Ba_2BiTaO_6 thin films by PLD.[43] The results confirmed the presence of high transparency (>90%) in the visible region and a high hole mobility of >30 $cm^2V^{-1}s^{-1}$, but carrier concentration is very limited by 5×10^{13} cm^{-3}. Nevertheless the Ba_2BiTaO_6 has a ubiquitous perovskite structure, which offers a wide range of possibility of integrations with other functional perovskite materials. This research highlights the importance of high-throughput computations to provide material scientists with new angles to attack the challenge in materials discovery.[183]

8. NiO ($3d^8$)

NiO is a well-known p-type semiconductor with a rocksalt type crystal structure and an optical bandgap of around 3.4-4.0 eV.[184] It is actually the first known p-TCO as reported by H. Sato *et al.* in 1993, who prepared $Ni_{1-x}O$ thin films by RF magnetron sputtering.[185] Their films show a conductivity up to 7.1 S cm^{-1} and a moderate transmittance of 40% in the visible region. Stoichiometric NiO is highly insulating. The p-type conductivity is believed due to hole states induced by Ni vacancies (V_{Ni}) formed in oxygen rich conditions. Doping NiO with Li^+ at Ni sites ($Li_xNi_{1-x}O$) is another way to enhance conductivity and has been extensively studied for a long time.[186-188] It was found if the doping is less than 0.25, the Li^+ ions randomly replace Ni sites without change the crystal structure. Each Li^+ ions in principle donates one hole state to the top of VB, although whether the hole state is of Ni^{3+} or O character is a matter of much debate because of the strong electron correlation in this system.[186, 189, 190] Electron correlations resulting from the nature of Ni 3d orbitals is a main factor limiting the conductivity of $Ni_{1-x}O$ or $Li_xNi_{1-x}O$. The highest conductivities reported for $Ni_{1-x}O$ and $Li_xNi_{1-x}O$ are 7.1 S cm^{-1}.[188, 191] All the temperature dependent conductivity show thermally activated Arrhenius behaviour. It is still debated whether the conduction is through a band-like or small polaron mechanism.[192] Chen et al. reported a high p-type Hall mobility of 28.56 cm^2/Vs could been achieved by RF sputtering [193]. However, one should keep in mind that to get a reliable hall mobility on p-type oxides is a nontrivial problem. Regardless of its low conductivity, NiO is likely the most widely used p-type TCOs. Similar to others p-TCOs discussed above, NiO has been used in electronic devices, such as TFTs and p–n diodes.[194-197] The simple rocksalt structure is one of the advantage for NiO, as this makes it more compatible to be integrated with other n-type materials. Ohta *et al.* have fabricated all single-crystalline transparent p-n heterojunction diode composed of p-NiO and n-ZnO epitaxially grown on YSZ(111) substrates by PLD. The diode exhibited clear rectifying I-V characteristics with a forward threshold voltage of 1 V. Efficient UV response

was observed up to 0.3 A W^{-1} at 360 nm, comparable to those of commercial GaN UV detectors.[195] Apart from these, NiO also shows promising applications in electrochromics for smart windows [198, 199], resistive switching memory[200, 201], and hole transport layer for solar cells.[202, 203]

9. Summary and remarks

In this article, we provided a review on the fundamental materials physics of traditional and recently emergent p-type TCOs, including Cu $3d^{10}$, Ni $3d^8$, nd^6, Cr $3d^3$ and post transition metal ns^2 based oxide materials. In essence, the key strategy for achieving a superior p-type TCO is to delocalize the top of VB by enhancing the orbital hybridization between O 2p and metal cations. This field has witnessed a steady development since the seminal report by Hosono and co-workers in 1997. Remarkable advances in transparent oxide semiconductor for (opto-)electronic devices have been achieved by using p-type TCOs or along with traditional n-type ones for transistors, UV LED and lasers, detectors and photovoltaics. However, the overall performance of p-TCOs is still far behind their n-type counterparts, as illustrated in Figure 5. Using anions (such as S^{2-}, Se^{2-}, P^{3-}) with *p*-orbitals more delocalized than oxygen and post transition metal ns^2 lone pair states (Sn^{2+}, Pb^{2+} and Bi^{3+}) would be a promising way for design of new p-type materials with superior performance. Meanwhile, the use of high-throughput computations also provide scientists with new angles to design materials in a more rational way. This is manifested by the initial study by G. Hautier *et al.* who screened over 3000 compounds and identified Ba_2BiTaO_6.[26, 43] Another recent computational screening by Yan *et al.* lead to the identification of TaIrGe (half-Heusler) as a new p-type TCO with a bandgap of 3.36 eV and remarkably high hole mobility of 2730 cm^2/Vs.[204]

Additionally we also discussed the chemistry of defects/doping in these materials based on recent computational simulations and experimental data. There are satisfactory

understandings in literatures on the microscopic mechanism of the energetics of defects, the transition energy levels, and the corresponding macroscopic transport properties. A domain remains largely unexplored but of particular interest is the surface and interface chemistry of the p-type TCOs, especially Cu_2O and SnO.[42, 63] Many research works have implied that the trap states formed at the interface are the key factor limiting the use of these materials for TFT and photovoltaic cells.[77, 78, 80]

Lastly we would like to point out that the selection criteria for p-type TCOs should be tightly related to the purpose of its applications. For (opto-)electronic devices such as transparent TFT and p-n diodes, a high mobility but low hole concentration is preferred. For use as hole transport layer in photovoltaic cells, a high hole conductivity and transparency for violet to near-infrared wavelengths become more important. This criteria does not require the materials directly have high mobility and visible light transparency. Hole doped transition metal oxides emerge to meet this requirement, as these type of materials can be amendable to achieve a high hole carriers concentration at the d orbitals. For example n= 7.5×10^{21} cm^{-3} and 2.2×10^{22} cm^{-3} have been achieved in Sr doped $LaCrO_3$[164] and $SrVO_3$,[205] respectively, while transparency is still maintained by the dipole forbidden transitions.

Acknowledgements

K.H.L. Zhang acknowledges the funding support from Herchel Smith Postdoctoral Fellowship by University of Cambridge.

Table I. A brief summary of major p-type TCOs reported in the literature. PLD: pulsed laser deposition; d: film thickness; T: transmittance in visible range; E_{opt}: optical bandgaps; σ: conductivity; n: carrier concentration; (some of the values are calculated by the authors according to $\sigma = ne\mu$); μ: hall mobility; FoM^H: figure of merit by Haackle; and FoM^G: figure of merits by Gordon. The parameters for ITO are typical value for conmercialized substrates.

Materials	Structure	Growth methods	d (nm)	T (%)	E_{opt} (eV)*	σ (S/cm)	n (cm^{-3})	μ (cm^2/Vs)	FoM^H	FoM^G	Ref
$Sn:In_2O_3$ (ITO)	Bixbyite	Sputtering	115	85	3.7	5900	1.2×10^{21}	30	13300	4×10^6	
Cu_2O	Cubic	PLD	650	–	2.17	0.014	1.7×10^{14}	90	–	–	63
$CuBO_2$	Delafossite	PLD	200	75	4.5	1.65	1×10^{17}	100	1.8	115	99
$CuAlO_2$	Delafossite	PLD	500	28	3.5	0.95	1.3×10^{17}	10.4	0.0002	37	25
$CuAlO_2$	Delafossite	PLD	230	70	3.5	0.34	2.7×10^{19}	0.13	0.22	21	27
$CuCr_{0.95}Mg_{0.05}O_2$	Delafossite	Sputtering	250	30	3.1	220	–	–	0.03	4570	28
$CuGaO_2$	Delafossite	PLD	300	80	3.6	0.02	1.7×10^{18}	0.23	0.2	8.4	33
$CuScO_{2+x}$	Delafossite	Sputtering	110	40	3.7	15	–	–	0.02	180	31
$CuIn_{0.93}Ca_{0.03}O_2$	Delafossite	PLD	100	40	3.7	0.006	–	–	0.001	0.14	30
$CuY_{1-x}Ca_xO_2$	Delafossite	Sputtering	100	41	3.5	1	–	–	0.003	27	32
$SrCu_2O_2$	Tetragonal	PLD	120	80	3.3	0.048	–	–	0.6	2.6	34
$La_{0.97}Sr_{0.03}CuOS$	Tetragonal	Sputtering	150	60	3.1	20	–	–	1.8	587	137
$La_{0.8}Mg_{0.2}CuOSe$	Tetragonal	Sputtering	40	–	2.8	910	1.7×10^{21}	3.5	–	–	144
$ZnRh_2O_4$	Spinel	PLD	100-300	55	2.74	2.75	–	–	0.13	91	41
$ZnIr_2O_4$	Spinel	PLD	100-300	61	2.97	3.39	–	–	0.47	136	41
$Mg_xCr_{2-x}O_3$	Corundum	Solution	150	65	3.3	0.33	–	–	0.07	11	163
$La_{0.75}Sr_{0.25}CrO_3$	Perovskite	MBE	80	55	4.6	15	3.4×10^{21}	0.03	0.26	196	164
$La_{0.50}Sr_{0.50}CrO_3$	Perovskite	MBE	50	43	4.6	56	7.5×10^{21}	0.04	0.05	326	164
SnO	Litharge	PLD	20	–	2.8	0.1	2.5×10^{17}	2.4	–	–	42
SnO	Litharge	Sputtering	200	0.85	2.8	0.77	1×10^{18}	4.8	3	95	178
Ba_2BiTaO_6	Perovskite	PLD	120	90	4.5	0.005	1×10^{14}	30	0.02	0.57	43
Li:NiO	Rocksalt	Sputtering	118	30	3.4	7.1	–	–	0.0005	70	185

Table II. Structural data, nearest-neighbor interatomic distances, bandgaps and calculated effective masses for the Cu*M*O_2 and Cu_2O; the numbers in brackets are the reference. The lattice parameters and interatomic distances are gathered from refs. [95-97]. * $CuGaO_2$, $CuScO_2$, $CuInO_2$, and $CuYO_2$ all have indirect bandgap according to DFT calculations (ref. [120]) and experimental optical transmission data. However there are no exact values reported so far.

	Cu_2O [58, 83]	**$CuBO_2$ [99,116]**	**$CuAlO_2$ [111, 113]**	**$CuCrO_2$ [104, 115]**	**$CuGaO_2$ [33]**	**$CuScO_2$ [31, 115]**	**$CuInO_2$ [104, 115]**	**$CuYO_2$ [32, 115]**
a (Å)	4.435	2.84	2.858	2.97	2.980	3.24	3.292	3.53
c (Å)	–	16.52	16.96	17.10	17.10	17.13	17.39	17.14
M^{3+} size (Å)	–	0.41	0.67	0.75	0.76	0.88	0.94	1.04
Cu-O (Å)	1.85	–	1.86	1.84	1.85	1.83	1.84	1.82
M-O (Å)	–	–	1.91	2.03	1.99	2.12	2.17	2.28
Cu-Cu (Å)	3.02	2.85	2.858	2.97	2.98	3.24	3.292	3.53
Direct E_g	2.17	4.5	3.47	3.1	3.6	3.3	3.9	3.5
Indirect E_g	–	2.2	2.97	2.5-2.6	NA*	NA*	NA*	NA*
m* [001]	0.24	1.71	38.95	6.07	NA	8.22	NA	7.64
m* [010]	0.24	0.45	2.6	4.53	NA	4.00	NA	3.72

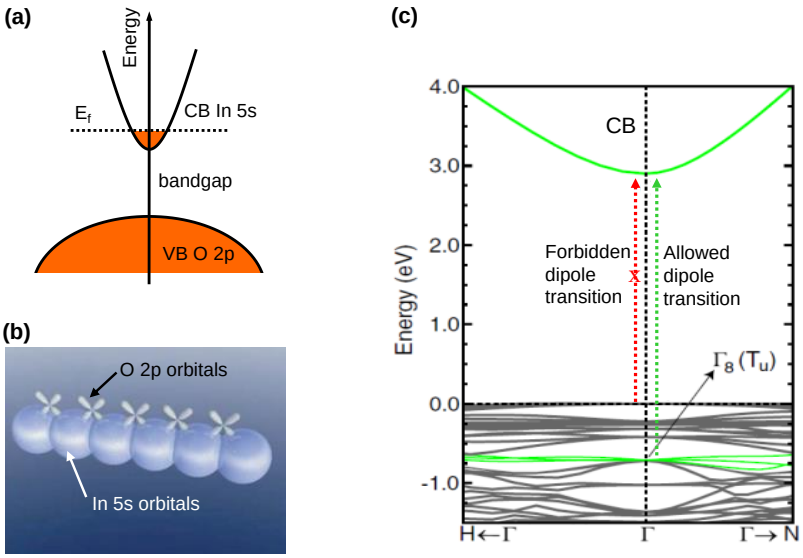

Figure 1. (a) schematic electronic structure of In_2O_3 doped with Sn, showing the In 5s derived conduction band (CB) and O 2p derived valence band (VB); (b) schematic orbital drawings for In_2O_3; large spheres denote In 5*s* orbitals, showing direct overlap between neighbouring *s* orbitals; the contribution of oxygen 2*p* orbitals is small. (Figure reproduced from ref [10]) (c) density functional theory (DFT) calculated bandstructure of In_2O_3 (Figure reproduced from ref [44])

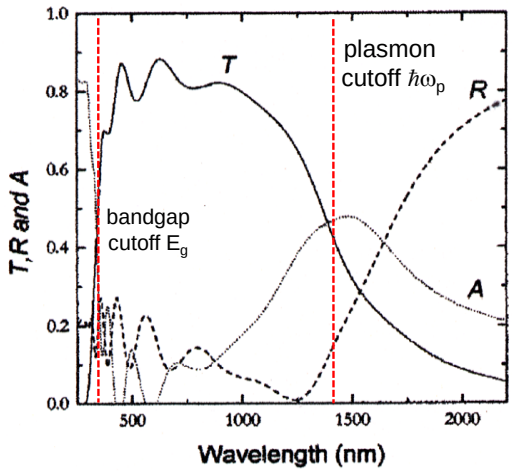

Figure 2 The "optical window" of TCOs set by its plasma edge ($\hbar\omega_p$) at longer wavelengths (lower energy) and optical bandgap at short wavelengths (high energy). (Figure adapted from ref [7])

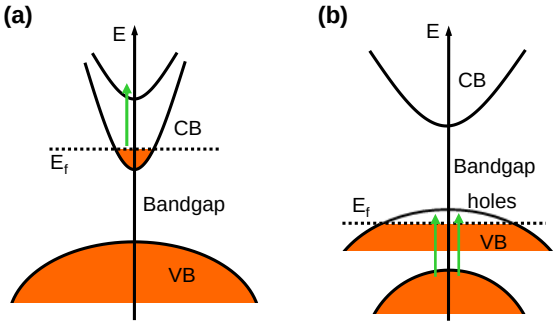

Figure 3. new transitions in highly doped TCOs, as marked by green arrows; (a) for n-TCOs, electronic transitions from CB to higher energy states. (b), for p-TCOs, electronic transitions from lower energy states to the hole state created at the top of VB.

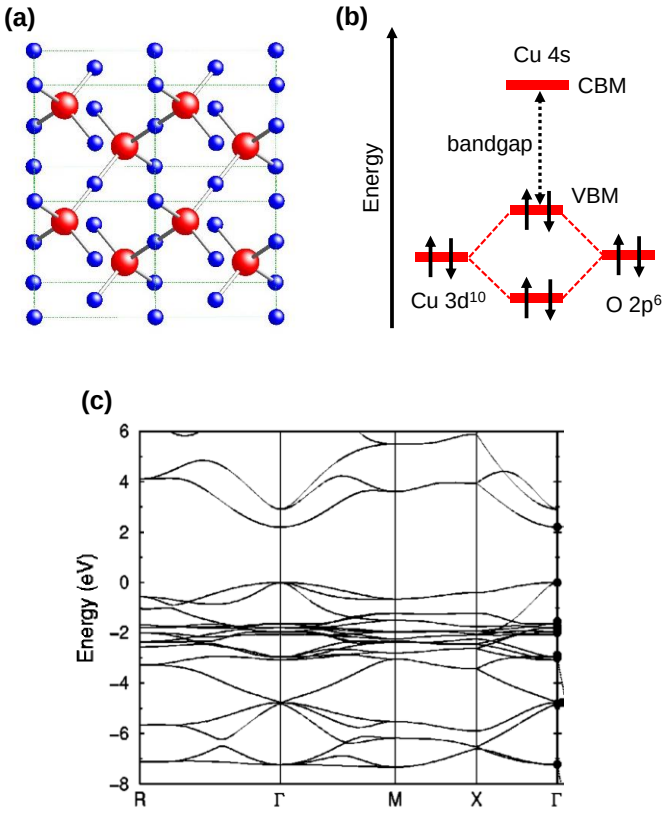

Figure 4. (a) crystal structure of Cu_2O; large red balls denote oxygen and small blue balls for Cu; (b) schematic energy diagram showing the hybridization of O 2p with Cu 3d; (c) LDA calculated bandstructure of Cu_2O by Nie *et al.* (Figure adapted from ref [83])

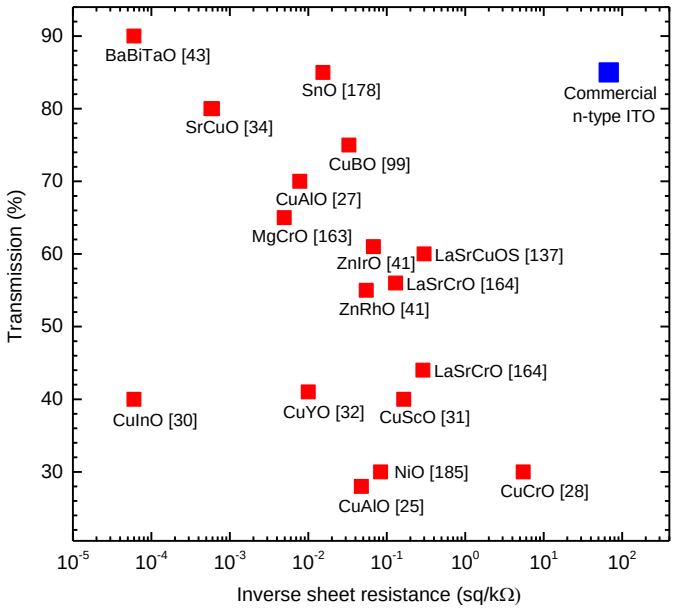

Figure 5. Graphical summary of optical transmission and inverse sheet resistance of the representative p-type TCOs in the literature (red squares) and commercial n-type ITO. The numbers in brackets are the reference.

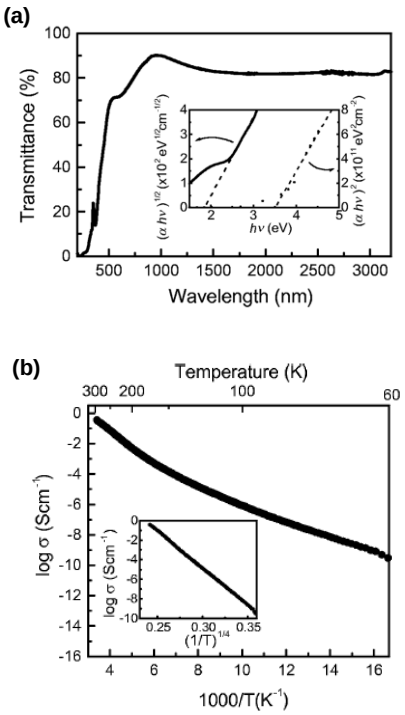

Figure 6. (a) optical transmission spectrum of $CuAlO_2$ thin film (the film thickness is 230 nm); The inset shows the plots of $(ah\gamma)^{1/2}$ vs $h\gamma$ and $(ah\gamma)^2$ vs $h\gamma$ for estimation of indirect and direct bandgap of $CuAlO_2$; (b) Arrhenius plots of electrical conductivity of $CuAlO_2$ thin film as function of temperature. Figures adapted from ref. [27]

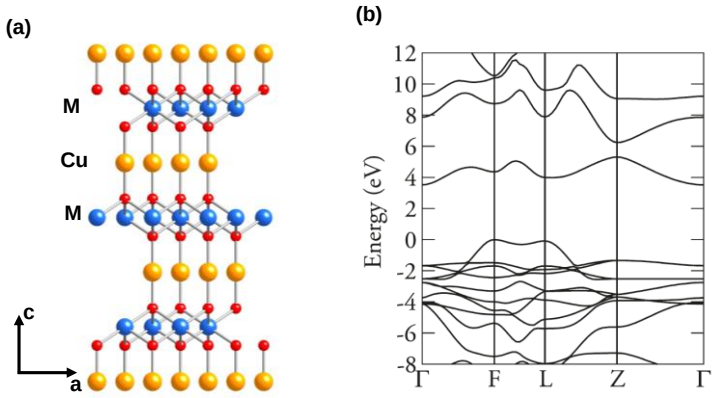

Figure 7. (a) crystal structure of CuMO_2; (b) HSE06 calculated bandstructure of $CuAlO_2$, plotted with reference to the top of the VB (0 eV); it clearly shows the dispersion of VBM at F- and L- point. The CBM is found at the Γ-point, making it an indirect bandgap materials. Calculation also show the VBM is derived from hybridized Cu 3d and O 2p orbitals, while the CBM is a mixture of Cu 4s and 3d with O 2p orbitals. (Figure adapted from ref [113])

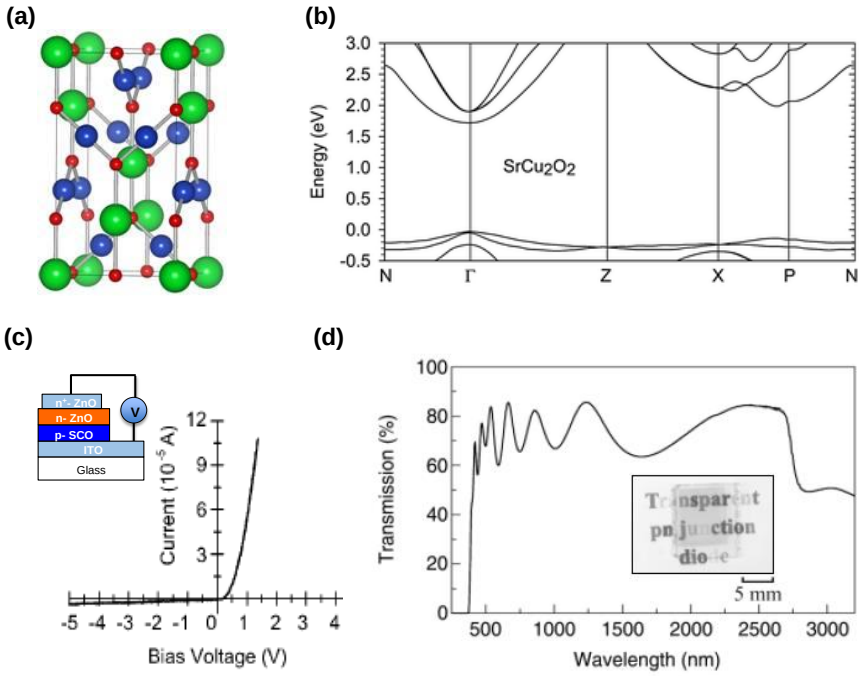

Figure 8. (a) The crystal structures of $SrCu_2O_2$; the Sr atoms are represented by large blue spheres, Cu ions by medium spheres and O ions by small spheres. (b) The bandstructure of $SrCu_2O_2$ along the high symmetry directions, plotted with reference to the top of the VB (0 eV). Both the VBM and CBM occur at the Γ point making it a direct gap material. (Figure adapted from ref [129]). (c)The structure and rectifying I–V characteristics of a transparent p-n heterojunction diode: glass/ITO/p-$SrCu_2O_2$/n-ZnO/n^+-ZnO. ITO and degenerately doped n^+-ZnO are used as ohmic contacts. (d) The optical transmission spectrum and photograph (inset) of the heterojunctions. (Figures adapted from ref [131])

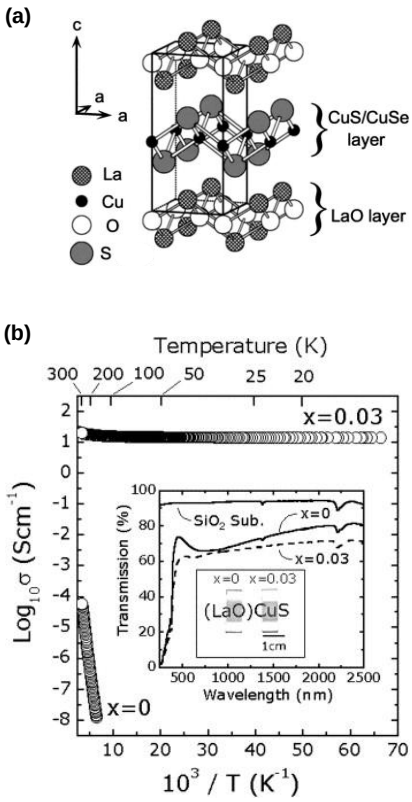

Figure 9. (a) Crystal structure of LaCuOS; where the LaO layer can be replaced by SrO leading to hole doping. (b) Temperature dependence of electrical conductivity for $La_{1-x}Sr_xCuOS$ films (x=0 and 0.03). The inset shows optical transmission spectra of the films in the visible–near IR region, and photographs. (Figure adapted from refs [137] and [143])

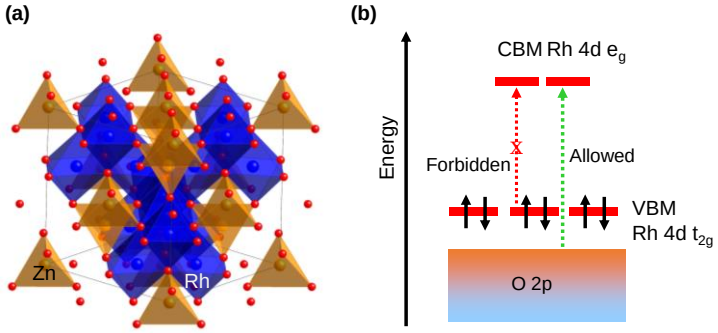

Figure 10. (a) Crystal structure of $ZnRh_2O_6$, where the Rh cations are coordinated by oxygen octahedrons (blue) and Zn in tetrahedrons (golden). (b) schematic energy diagram for the Rh $3d^6$ in oxygen octahedrons.

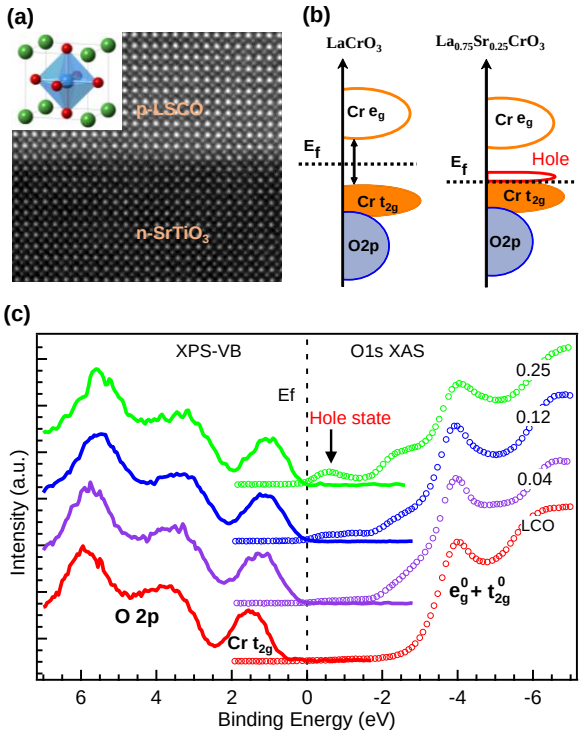

Figure 11. (a) A cross-sectional HRTEM image of the $La_{0.75}Sr_{0.25}CrO_3$ grown on $SrTiO_3$ (001) substrate. Inset shows the crystal structure of a perovskite. (b) Schematic energy diagram for $LaCrO_3$ and $La_{0.75}Sr_{0.25}CrO_3$. (c) Combination of XPS VB (left) and O K-edge XAS spectra (right) to map out the evolution of electronic structure of $La_{1-x}Sr_xCrO_3$ as function of Sr doping. The intensity of hole state at the top of VB increase with increasing of Sr doping. (Figure adapted for ref. [164])

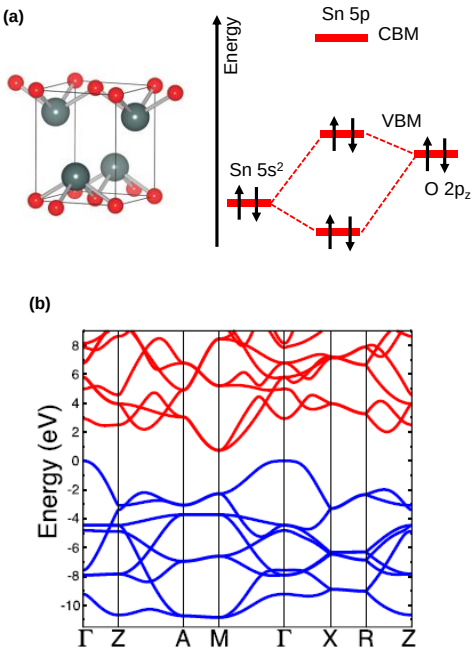

Figure 12. (a) Crystal structure and energy diagram of SnO; (b) Bandstructure of SnO along high-symmetry directions calculated with the HSE hybrid functional, showing indirect bandgap. (Figure adapted from ref. [181]).

Reference:

1. X. G. Yu, T. J. Marks and A. Facchetti, Nat. Mater. **15** (4), 383-396 (2016).
2. K. Ellmer, Nat. Photonics **6** (12), 808-816 (2012).
3. E. Fortunato, D. Ginley, H. Hosono and D. C. Paine, MRS Bull. **32** (3), 242-247 (2007).
4. R. M. P. Barquinha, L. Pereira and E. Fortunato, Transparent Oxide Electronics: From Materials to Devices, Wiley, 1st edition (2012).
5. T. Minami, Semicond. Sci. Technol. **20** (4), S35-S44 (2005).
6. C. G. Granqvist, Sol. Energy Mater. Sol. Cells **91** (17), 1529-1598 (2007).
7. G. Frank, E. Kauer and H. Kostlin, Thin Solid Films **77** (1-3), 107-117 (1981).
8. R. L. Hoffman, B. J. Norris and J. F. Wager, Appl. Phys. Lett. **82** (5), 733-735 (2003).
9. K. Nomura, H. Ohta, K. Ueda, T. Kamiya, M. Hirano and H. Hosono, Science **300** (5623), 1269-1272 (2003).
10. K. Nomura, H. Ohta, A. Takagi, T. Kamiya, M. Hirano and H. Hosono, Nature **432** (7016), 488-492 (2004).
11. E. Fortunato, P. Barquinha and R. Martins, Adv. Mater. **24** (22), 2945-2986 (2012).
12. H. Ohta and H. Hosono, Mater. Today **7** (6), 42-51 (2004).
13. Z. W. Pan, Z. R. Dai and Z. L. Wang, Science **291** (5510), 1947-1949 (2001).
14. E. Comini, G. Faglia, G. Sberveglieri, Z. W. Pan and Z. L. Wang, Appl. Phys. Lett. **81** (10), 1869-1871 (2002).
15. M. Batzill and U. Diebold, Prog. Surf. Sci. **79** (2-4), 47-154 (2005).
16. K. Baedeker, Annalen der Physik (Leipzig) **327**, 749 (1907).
17. J. J. Mudd, T. L. Lee, V. Munoz-Sanjose, J. Zuniga-Perez, D. Hesp, J. M. Kahk, D. J. Payne, R. G. Egdell and C. F. McConville, Phys. Rev. B **89** (3), 6 (2014).
18. P. D. C. King, T. D. Veal, C. F. McConville, J. Zuniga-Perez, V. Munoz-Sanjose, M. Hopkinson, E. D. L. Rienks, M. F. Jensen and P. Hofmann, Phys. Rev. Lett. **104** (25), 4 (2010).
19. M. A. McMaster, (Libby-Owens-Ford) (filed Oct. 5, 1942) U.S. Patent **2429** (1947).
20. P. P. Edwards, A. Porch, M. O. Jones, D. V. Morgan and R. M. Perks, Dalton Trans. (19), 2995-3002 (2004).
21. G. J. Exarhos and X. D. Zhou, Thin Solid Films **515** (18), 7025-7052 (2007).
22. K. P. Loh, Q. L. Bao, G. Eda and M. Chhowalla, Nat. Chem. **2** (12), 1015-1024 (2010).
23. H. Kawazoe, H. Yanagi, K. Ueda and H. Hosono, MRS Bull. **25** (8), 28-36 (2000).
24. A. N. Banerjee and K. K. Chattopadhyay, Prog. Cryst. Growth Charact. Mater. **50** (1-3), 52-105 (2005).
25. H. Kawazoe, M. Yasukawa, H. Hyodo, M. Kurita, H. Yanagi and H. Hosono, Nature **389** (6654), 939-942 (1997).
26. G. Hautier, A. Miglio, G. Ceder, G. M. Rignanese and X. Gonze, Nat. Commun. **4**, 7 (2013).

27. H. Yanagi, S. Inoue, K. Ueda, H. Kawazoe, H. Hosono and N. Hamada, J. Appl. Phys. **88** (7), 4159-4163 (2000).
28. R. Nagarajan, A. D. Draeseke, A. W. Sleight and J. Tate, J. Appl. Phys. **89** (12), 8022-8025 (2001).
29. T. Arnold, D. J. Payne, A. Bourlange, J. P. Hu, R. G. Egdell, L. F. J. Piper, L. Colakerol, A. Masi, P. A. Glans, T. Learmonth, K. E. Smith, J. Guo, D. O. Scanlon, A. Walsh, B. J. Morgan and G. W. Watson, Phys. Rev. B **79** (7), 9 (2009).
30. H. Yanagi, T. Hase, S. Ibuki, K. Ueda and H. Hosono, Appl. Phys. Lett. **78** (11), 1583-1585 (2001).
31. N. Duan, A. W. Sleight, M. K. Jayaraj and J. Tate, Appl. Phys. Lett. **77** (9), 1325-1326 (2000).
32. M. K. Jayaraj, A. D. Draeseke, J. Tate and A. W. Sleight, Thin Solid Films **397** (1-2), 244-248 (2001).
33. K. Ueda, T. Hase, H. Yanagi, H. Kawazoe, H. Hosono, H. Ohta, M. Orita and M. Hirano, J. Appl. Phys. **89** (3), 1790-1793 (2001).
34. A. Kudo, H. Yanagi, H. Hosono and H. Kawazoe, Appl. Phys. Lett. **73** (2), 220-222 (1998).
35. H. Ohta, K. Kawamura, M. Orita, M. Hirano, N. Sarukura and H. Hosono, Appl. Phys. Lett. **77** (4), 475-477 (2000).
36. K. Ueda, S. Inoue, S. Hirose, H. Kawazoe and H. Hosono, Appl. Phys. Lett. **77** (17), 2701-2703 (2000).
37. K. Ueda, S. Inoue, H. Hosono, N. Sarukura and M. Hirano, Appl. Phys. Lett. **78** (16), 2333-2335 (2001).
38. H. Hiramatsu, K. Ueda, H. Ohta, M. Hirano, T. Kamiya and H. Hosono, Appl. Phys. Lett. **82** (7), 1048-1050 (2003).
39. J. P. Allen, D. O. Scanlon, L. F. J. Piper and G. W. Watson, J. Mater. Chem. C **1** (48), 8194-8208 (2013).
40. M. L. Liu, L. B. Wu, Q. Huang, L. D. Chen and I. W. Chen, J. Appl. Phys. **102** (11), 3 (2007).
41. M. Dekkers, G. Rijnders and D. H. A. Blank, Appl. Phys. Lett. **90** (2), 3 (2007).
42. Y. Ogo, H. Hiramatsu, K. Nomura, H. Yanagi, T. Kamiya, M. Hirano and H. Hosono, Appl. Phys. Lett. **93** (3), 3 (2008).
43. A. Bhatia, G. Hautier, T. Nilgianskul, A. Miglio, J. Y. Sun, H. J. Kim, K. H. Kim, S. Chen, G. M. Rignanese, X. Gonze and J. Suntivich, Chem. Mat. **28** (1), 30-34 (2016).
44. A. Walsh, J. L. F. Da Silva, S. H. Wei, C. Korber, A. Klein, L. F. J. Piper, A. DeMasi, K. E. Smith, G. Panaccione, P. Torelli, D. J. Payne, A. Bourlange and R. G. Egdell, Phys. Rev. Lett. **100** (16), 4 (2008).
45. K. H. L. Zhang, V. K. Lazarov, T. D. Veal, F. E. Oropeza, C. F. McConville, R. G. Egdell and A. Walsh, J. Phys.-Condes. Matter **23** (33), 8 (2011).
46. J. L. Lyons, A. Janotti and C. G. Van de Walle, Appl. Phys. Lett. **95** (25), 3 (2009).
47. J. C. Fan, K. M. Sreekanth, Z. Xie, S. L. Chang and K. V. Rao, Prog. Mater. Sci. **58** (6), 874-985 (2013).

48. O. Bierwagen and J. S. Speck, Appl. Phys. Lett. **101** (10), 4 (2012).
49. K. H. L. Zhang, R. G. Egdell, F. Offi, S. Iacobucci, L. Petaccia, S. Gorovikov and P. D. C. King, Phys. Rev. Lett. **110** (5), 5 (2013).
50. G. Haacke, J. Appl. Phys. **47** (9), 4086-4089 (1976).
51. R. G. Gordon, MRS Bull. **25** (8), 52-57 (2000).
52. A. Zunger, Appl. Phys. Lett. **83** (1), 57-59 (2003).
53. S. B. Zhang, S. H. Wei and A. Zunger, Phys. Rev. B **63** (7), 7 (2001).
54. S. B. Zhang, S. H. Wei and A. Zunger, J. Appl. Phys. **83** (6), 3192-3196 (1998).
55. J. Robertson and S. J. Clark, Phys. Rev. B **83** (7), 7 (2011).
56. B. K. Meyer, A. Polity, D. Reppin, M. Becker, P. Hering, B. Kramm, P. J. Klar, T. Sander, C. Reindl, C. Heiliger, M. Heinemann, C. Muller and C. Ronning, in *Oxide Semiconductors*, edited by B. G. Svensson, S. J. Pearton and C. Jagadish (Elsevier Academic Press Inc, San Diego, 2013), Vol. 88, pp. 201-226.
57. J. M. Zuo, M. Kim, M. O'Keeffe and J. C. H. Spence, Nature **401** (6748), 49-52 (1999).
58. A. Buljan, M. Llunell, E. Ruiz and P. Alemany, Chem. Mat. **13** (2), 338-344 (2001).
59. B. P. Rai, Solar Cells **25** (3), 265-272 (1988).
60. J. Katayama, K. Ito, M. Matsuoka and J. Tamaki, J. Appl. Electrochem. **34** (7), 687-692 (2004).
61. A. Paracchino, V. Laporte, K. Sivula, M. Gratzel and E. Thimsen, Nat. Mater. **10** (6), 456-461 (2011).
62. B. K. Meyer, A. Polity, D. Reppin, M. Becker, P. Hering, P. J. Klar, T. Sander, C. Reindl, J. Benz, M. Eickhoff, C. Heiliger, M. Heinemann, J. Blasing, A. Krost, S. Shokovets, C. Muller and C. Ronning, Phys. Status Solidi B-Basic Solid State Phys. **249** (8), 1487-1509 (2012).
63. K. Matsuzaki, K. Nomura, H. Yanagi, T. Kamiya, M. Hirano and H. Hosono, Appl. Phys. Lett. **93** (20), 3 (2008).
64. E. Fortunato, V. Figueiredo, P. Barquinha, E. Elamurugu, R. Barros, G. Goncalves, S. H. K. Park, C. S. Hwang and R. Martins, Appl. Phys. Lett. **96** (19), 3 (2010).
65. K. R. Balasubramaniam, V. M. Kao, J. Ravichandran, P. B. Rossen, W. Siemons and J. W. Ager, Thin Solid Films **520** (11), 3914-3917 (2012).
66. W. Seiler, E. Millon, J. Perriere, R. Benzerga and C. Boulmer-Leborgne, J. Cryst. Growth **311** (12), 3352-3358 (2009).
67. B. S. Li, K. Akimoto and A. Shen, J. Cryst. Growth **311** (4), 1102-1105 (2009).
68. D. W. Nam, I. T. Cho, J. H. Lee, E. S. Cho, J. Sohn, S. H. Song and H. I. Kwon, J. Vac. Sci. Technol. B **30** (6), 5 (2012).
69. K. J. Saji, S. Populoh, A. N. Tiwari and Y. E. Romanyuk, Phys. Status Solidi A-Appl. Mat. **210** (7), 1386-1391 (2013).
70. Y. S. Lee, M. T. Winkler, S. C. Siah, R. Brandt and T. Buonassisi, Appl. Phys. Lett. **98** (19), 3 (2011).
71. T. Minami, Y. Nishi and T. Miyata, Appl. Phys. Lett. **105** (21), 5 (2014).
72. T. Minami, Y. Nishi, T. Miyata and J. Nomoto, Appl. Phys. Express **4** (6), 3 (2011).

73. S. Y. Kim, C. H. Ahn, J. H. Lee, Y. H. Kwon, S. Hwang, J. Y. Lee and H. K. Cho, ACS Appl. Mater. Interfaces **5** (7), 2417-2421 (2013).
74. H. Nagai, T. Suzuki, H. Hara, C. Mochizuki, I. Takano, T. Honda and M. Sato, Mater. Chem. Phys. **137** (1), 252-257 (2012).
75. D. Munoz-Rojas, M. Jordan, C. Yeoh, A. T. Marin, A. Kursumovic, L. A. Dunlop, D. C. Iza, A. Chen, H. Wang and J. L. M. Driscoll, AIP Adv. **2** (4), 7 (2012).
76. L. Bergerot, C. Jimenez, O. Chaix-Pluchery, L. Rapenne and J. L. Deschanvres, Phys. Status Solidi A-Appl. Mat. **212** (8), 1735-1741 (2015).
77. F. Y. Ran, H. Hiramatsu, H. Hosono, T. Kamiya and M. Taniguti, J. Vac. Sci. Technol. B **33** (5), 6 (2015).
78. S. W. Lee, Y. S. Lee, J. Heo, S. C. Siah, D. Chua, R. E. Brandt, S. B. Kim, J. P. Mailoa, T. Buonassisi and R. G. Gordon, Adv. Energy Mater. **4** (11), 7 (2014).
79. R. L. Z. Hoye, R. E. Brandt, Y. Ievskaya, S. Heffernan, K. P. Musselman, T. Buonassisi and J. L. MacManus-Driscoll, APL Mater. **3** (2), 4 (2015).
80. Y. S. Lee, D. Chua, R. E. Brandt, S. C. Siah, J. V. Li, J. P. Mailoa, S. W. Lee, R. G. Gordon and T. Buonassisi, Adv. Mater. **26** (27), 4704-+ (2014).
81. J. P. Hu, D. J. Payne, R. G. Egdell, P. A. Glans, T. Learmonth, K. E. Smith, J. Guo and N. M. Harrison, Phys. Rev. B **77** (15), 10 (2008).
82. E. Ruiz, S. Alvarez, P. Alemany and R. A. Evarestov, Phys. Rev. B **56** (12), 7189-7196 (1997).
83. X. L. Nie, S. H. Wei and S. B. Zhang, Phys. Rev. B **65** (7), 8 (2002).
84. J. W. Hodby, T. E. Jenkins, C. Schwab, H. Tamura and D. Trivich, Journal Of Physics C-Solid State Physics **9** (8), 1429-1439 (1976).
85. H. Raebiger, S. Lany and A. Zunger, Phys. Rev. B **76** (4), 5 (2007).
86. D. O. Scanlon, B. J. Morgan, G. W. Watson and A. Walsh, Phys. Rev. Lett. **103** (9), 4 (2009).
87. A. F. Wright and J. S. Nelson, J. Appl. Phys. **92** (10), 5849-5851 (2002).
88. F. Ameena, The University of Texas at Arlington, PhD thesis (2012).
89. M. Nolan, Thin Solid Films **516** (22), 8130-8135 (2008).
90. D. O. Scanlon, B. J. Morgan and G. W. Watson, J. Chem. Phys. **131** (12), 8 (2009).
91. A. E. Rakhshani, Y. Makdisi and X. Mathew, Thin Solid Films **288** (1-2), 69-75 (1996).
92. G. K. Paul, Y. Nawa, H. Sato, T. Sakurai and K. Akimoto, Appl. Phys. Lett. **88** (14), 3 (2006).
93. G. K. Paul, R. Ghosh, S. K. Bera, S. Bandyopadhyay, T. Sakurai and K. Akimoto, Chem. Phys. Lett. **463** (1-3), 117-120 (2008).
94. A. Bose, S. Basu, S. Banerjee and D. Chakravorty, J. Appl. Phys. **98** (7), 5 (2005).
95. B. U. Kohler and M. Jansen, Z. Anorg. Allg. Chem. **543** (12), 73-80 (1986).
96. M. Trari, J. Topfer, J. P. Doumerc, M. Pouchard, A. Ammar and P. Hagenmuller, J. Solid State Chem. **111** (1), 104-110 (1994).
97. R. D. Shannon, D. B. Rogers and C. T. Prewitt, Inorg. Chem. **10** (4), 713-& (1971).

98. B. J. Ingram, G. B. Gonzalez, T. O. Mason, D. Y. Shahriari, A. Barnabe, D. G. Ko and K. R. Poeppelmeier, Chem. Mat. **16** (26), 5616-5622 (2004).
99. M. Snure and A. Tiwari, Appl. Phys. Lett. **91** (9), 3 (2007).
100. C. Ruttanapun, J. Appl. Phys. **114** (11), 5 (2013).
101. Y. Kakehi, K. Satoh, T. Yotsuya, K. Masuko, T. Yoshimura, A. Ashida and N. Fujimura, J. Cryst. Growth **311** (4), 1117-1122 (2009).
102. M. Singh, V. N. Singh and B. R. Mehta, J. Nanosci. Nanotechnol. **8** (8), 3889-3894 (2008).
103. A. Barnabe, Y. Thimont, M. Lalanne, L. Presmanes and P. Tailhades, J. Mater. Chem. C **3** (23), 6012-6024 (2015).
104. D. Shin, J. S. Foord, R. G. Egdell and A. Walsh, J. Appl. Phys. **112** (11), 7 (2012).
105. X. R. Li, M. J. Han, X. L. Zhang, C. Shan, Z. G. Hu, Z. Q. Zhu and J. H. Chu, Phys. Rev. B **90** (3), 8 (2014).
106. M. J. Han, Z. H. Duan, J. Z. Zhang, S. Zhang, Y. W. Li, Z. G. Hu and J. H. Chu, J. Appl. Phys. **114** (16), 9 (2013).
107. M. J. Han, K. Jiang, J. Z. Zhang, W. L. Yu, Y. W. Li, Z. G. Hu and J. H. Chu, J. Mater. Chem. **22** (35), 18463-18470 (2012).
108. D. J. Aston, D. J. Payne, A. J. H. Green, R. G. Egdell, D. S. L. Law, J. Guo, P. A. Glans, T. Learmonth and K. E. Smith, Phys. Rev. B **72** (19), 9 (2005).
109. H. M. Luo, M. Jain, T. M. McCleskey, E. Bauer, A. K. Burrell and Q. X. Jia, Adv. Mater. **19** (21), 3604-+ (2007).
110. R. Nagarajan, N. Duan, M. K. Jayaraj, J. Li, K. A. Vanaja, A. Yokochi, A. Draeseke, J. Tate and A. W. Sleight, Int. J. Inorg. Mater. **3** (3), 265-270 (2001).
111. J. Tate, H. L. Ju, J. C. Moon, A. Zakutayev, A. P. Richard, J. Russell and D. H. McIntyre, Phys. Rev. B **80** (16), 8 (2009).
112. W. Ketir, S. Saadi and M. Trari, J. Solid State Electrochem. **16** (1), 213-218 (2012).
113. D. O. Scanlon and G. W. Watson, J. Phys. Chem. Lett. **1** (21), 3195-3199 (2010).
114. D. O. Scanlon and G. W. Watson, J. Mater. Chem. **21** (11), 3655-3663 (2011).
115. D. O. Scanlon, K. G. Godinho, B. J. Morgan and G. W. Watson, J. Chem. Phys. **132** (2), 10 (2010).
116. D. O. Scanlon, A. Walsh and G. W. Watson, Chem. Mat. **21** (19), 4568-4576 (2009).
117. D. O. Scanlon, A. Walsh, B. J. Morgan, G. W. Watson, D. J. Payne and R. G. Egdell, Phys. Rev. B **79** (3), 7 (2009).
118. T. Okuda, N. Jufuku, S. Hidaka and N. Terada, Phys. Rev. B **72** (14), 5 (2005).
119. T. Yokobori, M. Okawa, K. Konishi, R. Takei, K. Katayama, S. Oozono, T. Shinmura, T. Okuda, H. Wadati, E. Sakai, K. Ono, H. Kumigashira, M. Oshima, T. Sugiyama, E. Ikenaga, N. Hamada and T. Saitoh, Phys. Rev. B **87** (19), 8 (2013).
120. X. L. Nie, S. H. Wei and S. B. Zhang, Phys. Rev. Lett. **88** (6), 4 (2002).
121. M. Singh, B. R. Mehta, D. Varandani and V. N. Singh, J. Appl. Phys. **106** (5), 6 (2009).
122. J. Pellicer-Porres, A. Segura, A. S. Gilliland, A. Munoz, P. Rodriguez-Hernendez, D. Kim, M. S. Lee and T. Y. Kim, Appl. Phys. Lett. **88** (18), 3 (2006).

123. H. Katayama-Yoshida, T. Koyanagi, H. Funashima, H. Harima and A. Yanase, Solid State Commun. **126** (3), 135-139 (2003).
124. I. Hamada and H. Katayama-Yoshida, Physica B **376**, 808-811 (2006).
125. B. J. Ingram, B. J. Harder, N. W. Hrabe and T. O. Mason, Chem. Mat. **16** (26), 5623-5629 (2004).
126. H. Ohta, M. Orita, M. Hirano, I. Yagi, K. Ueda and H. Hosono, J. Appl. Phys. **91** (5), 3074-3078 (2002).
127. J. P. Hu, D. J. Payne, R. G. Egdell, N. M. Harrison and V. R. Dhanak, Chem. Phys. Lett. **450** (1-3), 39-43 (2007).
128. C. C. B. Lynch, R. G. Egdell and D. S. L. Law, Chem. Phys. Lett. **401** (1-3), 223-226 (2005).
129. K. G. Godinho, J. J. Carey, B. J. Morgan, D. O. Scanlon and G. W. Watson, J. Mater. Chem. **20** (6), 1086-1096 (2010).
130. K. G. Godinho, G. W. Watson, A. Walsh, A. J. H. Green, D. J. Payne, J. Harmer and R. G. Egdell, J. Mater. Chem. **18** (24), 2798-2806 (2008).
131. A. Kudo, H. Yanagi, K. Ueda, H. Hosono, H. Kawazoe and Y. Yano, Appl. Phys. Lett. **75** (18), 2851-2853 (1999).
132. H. Ohta, M. Orita, M. Hirano and H. Hosono, J. Appl. Phys. **89** (10), 5720-5725 (2001).
133. K. Ishikawa, S. Kinoshita, Y. Suzuki, S. Matsuura, T. Nakanishi, M. Aizawa and Y. Suzuki, J. Electrochem. Soc. **138** (4), 1166-1170 (1991).
134. M. Palazzi, Comptes Rendus De L Academie Des Sciences Serie Ii **292** (10), 789-791 (1981).
135. S. Inoue, K. Ueda, H. Hosono and N. Hamada, Phys. Rev. B **64** (24), 5 (2001).
136. M. Imada, A. Fujimori and Y. Tokura, Rev. Mod. Phys. **70** (4), 1039-1263 (1998).
137. H. Hiramatsu, K. Ueda, H. Ohta, M. Orita, M. Hirano and H. Hosono, Thin Solid Films **411** (1), 125-128 (2002).
138. H. Hiramatsu, K. Ueda, H. Ohta, M. Orita, M. Hirano and H. Hosono, Appl. Phys. Lett. **81** (4), 598-600 (2002).
139. H. Hosono, Thin Solid Films **515** (15), 6000-6014 (2007).
140. Y. Goto, M. Tanaki, Y. Okusa, T. Shibuya, K. Yasuoka, M. Matoba and Y. Kamihara, Appl. Phys. Lett. **105** (2), 4 (2014).
141. K. Ueda, H. Hiramatsu, M. Hirano, T. Kamiya and H. Hosono, Thin Solid Films **496** (1), 8-15 (2006).
142. S. J. Clarke, P. Adamson, S. J. C. Herkelrath, O. J. Rutt, D. R. Parker, M. J. Pitcher and C. F. Smura, Inorg. Chem. **47** (19), 8473-8486 (2008).
143. K. Ueda and H. Hosono, J. Appl. Phys. **91** (7), 4768-4770 (2002).
144. H. Hiramatsu, K. Ueda, H. Ohta, M. Hirano, M. Kikuchi, H. Yanagi, T. Kamiya and H. Hosono, Appl. Phys. Lett. **91** (1), 3 (2007).
145. D. O. Scanlon and G. W. Watson, Chem. Mat. **21** (22), 5435-5442 (2009).
146. S. Narushima, H. Mizoguchi, K. Shimizu, K. Ueda, H. Ohta, M. Hirano, T. Kamiya and H. Hosono, Adv. Mater. **15** (17), 1409-1413 (2003).

147. H. Mizoguchi, M. Hirano, S. Fujitsu, T. Takeuchi, K. Ueda and H. Hosono, Appl. Phys. Lett. **80** (7), 1207-1209 (2002).
148. N. Mansourian-Hadavi, S. Wansom, N. H. Perry, A. R. Nagaraja, T. O. Mason, L. H. Ye and A. J. Freeman, Phys. Rev. B **81** (7), 6 (2010).
149. D. J. Singh, R. C. Rai, J. L. Musfeldt, S. Auluck, N. Singh, P. Khalifah, S. McClure and D. G. Mandrus, Chem. Mat. **18** (11), 2696-2700 (2006).
150. M. N. Amini, H. Dixit, R. Saniz, D. Lamoen and B. Partoens, Phys. Chem. Chem. Phys. **16** (6), 2588-2596 (2014).
151. D. O. Scanlon and G. W. Watson, Phys. Chem. Chem. Phys. **13** (20), 9667-9675 (2011).
152. T. W. Kim, M. A. Woo, M. Regis and K. S. Choi, J. Phys. Chem. Lett. **5** (13), 2370-2374 (2014).
153. X. J. Liu, Z. Chang, L. Luo, T. H. Xu, X. D. Lei, J. F. Liu and X. M. Sun, Chem. Mat. **26** (5), 1889-1895 (2014).
154. S. B. Wang, Z. X. Ding and X. C. Wang, Chem. Commun. **51** (8), 1517-1519 (2015).
155. J. B. Cheng, Y. Lu, K. W. Qiu, H. L. Yan, X. Y. Hou, J. Y. Xu, L. Han, X. M. Liu, J. K. Kim and Y. S. Luo, Phys. Chem. Chem. Phys. **17** (26), 17016-17022 (2015).
156. Y. Sharma, N. Sharma, G. V. S. Rao and B. V. R. Chowdari, Adv. Funct. Mater. **17** (15), 2855-2861 (2007).
157. R. B. Wu, X. K. Qian, K. Zhou, J. Wei, J. Lou and P. M. Ajayan, ACS Nano **8** (6), 6297-6303 (2014).
158. S. Kim, J. A. Cianfrone, P. Sadik, K. W. Kim, M. Ivill and D. P. Norton, J. Appl. Phys. **107** (10), 5 (2010).
159. F. L. Schein, M. Winter, T. Bontgen, H. von Wenckstern and M. Grundmann, Appl. Phys. Lett. **104** (2), 4 (2014).
160. P. Schlupp, F. L. Schein, H. von Wenckstern and M. Grundmann, Adv. Electron. Mater. **1** (1-2), 5 (2015).
161. F. J. Klupfel, A. Holtz, F. L. Schein, H. von Wenckstern and M. Grundmann, IEEE Trans. Electron Devices **62** (12), 4004-4008 (2015).
162. J. D. Perkins, T. R. Paudel, A. Zakutayev, P. F. Ndione, P. A. Parilla, D. L. Young, S. Lany, D. S. Ginley, A. Zunger, N. H. Perry, Y. Tang, M. Grayson, T. O. Mason, J. S. Bettinger, Y. Shi and M. F. Toney, Phys. Rev. B **84** (20), 8 (2011).
163. E. Arca, K. Fleischer and I. V. Shvets, Appl. Phys. Lett. **99** (11), 3 (2011).
164. K. H. L. Zhang, Y. G. Du, A. Papadogianni, O. Bierwagen, S. Sallis, L. F. J. Piper, M. E. Bowden, V. Shutthanandan, P. V. Sushko and S. A. Chambers, Adv. Mater. **27** (35), 5191-5195 (2015).
165. D. S. McClure, J. Chem. Phys. **38** (9), 2289-& (1963).
166. S. Lany, J. Phys.-Condes. Matter **27** (28), 18 (2015).
167. N. Uekawa and K. Kaneko, J. Phys. Chem. **100** (10), 4193-4198 (1996).
168. E. Norton, L. Farrell, S. D. Callaghan, C. McGuinness, I. V. Shvets and K. Fleischer, Phys. Rev. B **93** (11), 8 (2016).

169. L. Farrell, K. Fleischer, D. Caffrey, D. Mullarkey, E. Norton and I. V. Shvets, Phys. Rev. B **91** (12), 10 (2015).
170. P. V. Sushko, L. Qiao, M. Bowden, T. Varga, G. J. Exarhos, F. K. Urban, D. Barton and S. A. Chambers, Phys. Rev. Lett. **110** (7), 5 (2013).
171. K. H. L. Zhang, Y. Du, P. V. Sushko, M. E. Bowden, V. Shutthanandan, S. Sallis, L. F. J. Piper and S. A. Chambers, Phys. Rev. B **91** (15), 9 (2015).
172. S. A. Chambers, L. Qiao, T. C. Droubay, T. C. Kaspar, B. W. Arey and P. V. Sushko, Phys. Rev. Lett. **107** (20), 4 (2011).
173. A. Walsh, D. J. Payne, R. G. Egdell and G. W. Watson, Chem. Soc. Rev. **40** (9), 4455-4463 (2011).
174. A. Walsh and G. W. Watson, J. Solid State Chem. **178** (5), 1422-1428 (2005).
175. A. Walsh and G. W. Watson, Phys. Rev. B **70** (23), 7 (2004).
176. Y. Ogo, H. Hiramatsu, K. Nomura, H. Yanagi, T. Kamiya, M. Kimura, M. Hirano and H. Hosono, Phys. Status Solidi A-Appl. Mat. **206** (9), 2187-2191 (2009).
177. L. Y. Liang, H. T. Cao, X. B. Chen, Z. M. Liu, F. Zhuge, H. Luo, J. Li, Y. C. Lu and W. Lu, Appl. Phys. Lett. **100** (26), 5 (2012).
178. E. Fortunato, R. Barros, P. Barquinha, V. Figueiredo, S. H. K. Park, C. S. Hwang and R. Martins, Appl. Phys. Lett. **97** (5), 3 (2010).
179. H. Yabuta, N. Kaji, R. Hayashi, H. Kumomi, K. Nomura, T. Kamiya, M. Hirano and H. Hosono, Appl. Phys. Lett. **97** (7), 3 (2010).
180. N. F. Quackenbush, J. P. Allen, D. O. Scanlon, S. Sallis, J. A. Hewlett, A. S. Nandur, B. Chen, K. E. Smith, C. Weiland, D. A. Fischer, J. C. Woicik, B. E. White, G. W. Watson and L. F. J. Piper, Chem. Mat. **25** (15), 3114-3123 (2013).
181. J. B. Varley, A. Schleife, A. Janotti and C. G. Van de Walle, Appl. Phys. Lett. **103** (8), 4 (2013).
182. H. Hosono, Y. Ogo, H. Yanagi and T. Kamiya, Electrochem. Solid State Lett. **14** (1), II13-II16 (2011).
183. A. Jain, S. P. Ong, G. Hautier, W. Chen, W. D. Richards, S. Dacek, S. Cholia, D. Gunter, D. Skinner, G. Ceder and K. A. Persson, APL Mater. **1** (1), 11 (2013).
184. G. A. Sawatzky and J. W. Allen, Phys. Rev. Lett. **53** (24), 2339-2342 (1984).
185. H. Sato, T. Minami, S. Takata and T. Yamada, Thin Solid Films **236** (1-2), 27-31 (1993).
186. J. Vanelp, H. Eskes, P. Kuiper and G. A. Sawatzky, Phys. Rev. B **45** (4), 1612-1622 (1992).
187. J. B. Goodenough, D. G. Wickham and W. J. Croft, J. Phys. Chem. Solids **5** (1-2), 107-116 (1958).
188. T. Dutta, P. Gupta, A. Gupta and J. Narayan, J. Appl. Phys. **108** (8), 7 (2010).
189. P. Kuiper, G. Kruizinga, J. Ghijsen, G. A. Sawatzky and H. Verweij, Phys. Rev. Lett. **62** (2), 221-224 (1989).
190. I. J. Pickering, G. N. George, J. T. Lewandowski and A. J. Jacobson, J. Am. Chem. Soc. **115** (10), 4137-4144 (1993).
191. E. Antolini, Mater. Chem. Phys. **82** (3), 937-948 (2003).

192. A. J. Bosman and Crevecoe.C, Physical Review **144** (2), 763-& (1966).
193. S. C. Chen, C. K. We, T. Y. Kuo, W. C. Peng and H. C. Lin, Thin Solid Films **572**, 51-55 (2014).
194. R. K. Gupta, K. Ghosh and P. K. Kahol, Physica E **41** (4), 617-620 (2009).
195. H. Ohta, M. Hirano, K. Nakahara, H. Maruta, T. Tanabe, M. Kamiya, T. Kamiya and H. Hosono, Appl. Phys. Lett. **83** (5), 1029-1031 (2003).
196. W. Y. Lee, D. Mauri and C. Hwang, Appl. Phys. Lett. **72** (13), 1584-1586 (1998).
197. H. Ohta, M. Kamiya, T. Kamaiya, M. Hirano and H. Hosono, Thin Solid Films **445** (2), 317-321 (2003).
198. G. A. Niklasson and C. G. Granqvist, J. Mater. Chem. **17** (2), 127-156 (2007).
199. X. H. Xia, J. P. Tu, J. Zhang, X. L. Wang, W. K. Zhang and H. Huang, Sol. Energy Mater. Sol. Cells **92** (6), 628-633 (2008).
200. J. Y. Son and Y. H. Shin, Appl. Phys. Lett. **92** (22), 3 (2008).
201. M. J. Lee, S. Han, S. H. Jeon, B. H. Park, B. S. Kang, S. E. Ahn, K. H. Kim, C. B. Lee, C. J. Kim, I. K. Yoo, D. H. Seo, X. S. Li, J. B. Park, J. H. Lee and Y. Park, Nano Lett. **9** (4), 1476-1481 (2009).
202. J. J. He, H. Lindstrom, A. Hagfeldt and S. E. Lindquist, J. Phys. Chem. B **103** (42), 8940-8943 (1999).
203. M. D. Irwin, B. Buchholz, A. W. Hains, R. P. H. Chang and T. J. Marks, Proc. Natl. Acad. Sci. U. S. A. **105** (8), 2783-2787 (2008).
204. F. Yan, X. W. Zhang, Y. G. Yu, L. P. Yu, A. Nagaraja, T. O. Mason and A. Zunger, Nat. Commun. **6**, 8 (2015).
205. L. Zhang, Y. J. Zhou, L. Guo, W. W. Zhao, A. Barnes, H. T. Zhang, C. Eaton, Y. X. Zheng, M. Brahlek, H. F. Haneef, N. J. Podraza, M. H. W. Chan, V. Gopalan, K. M. Rabe and R. Engel-Herbert, Nat. Mater. **15** (2), 204-+ (2016).